Earth and Planetary Science Letters 556 (2021) 116725

Contents lists available at ScienceDirect

Earth and Planetary Science Letters

www.elsevier.com/locate/epsl

Mesoarchaean acidic volcanic lakes: A critical ecological niche in early land colonisation

Andrea Agangi [a,b,*], Axel Hofmann [a], Frantz Ossa Ossa [a,c], Dóra Paprika [a], Andrey Bekker [a,d]

[a] Department of Geology, University of Johannesburg, Auckland Park 2006, South Africa
[b] Department of Earth Resource Science, Akita University, Akita 010-8502, Japan
[c] Department of Geosciences, University of Tuebingen, 72074 Tuebingen, Germany
[d] Department of Earth and Planetary Sciences, University of California, Riverside, CA, 92521, USA

ARTICLE INFO

Article history:
Received 9 November 2020
Received in revised form 11 December 2020
Accepted 16 December 2020
Available online xxxx
Editor: F. Moynier

Keywords:
Dominion Group
Mesoarchaean
Kaapvaal Craton
early life

ABSTRACT

The antiquity of life in marine environments has been demonstrated, with examples of microfossils and stromatolites extending back to at least 3.5 billion years ago (Ga). In contrast, emerged land was likely a more challenging environment during the Archaean, and only sparse evidence of life in non-marine environments has so far been identified. Here we document the abundance of isotopically light carbon (with $\delta^{13}C$ values from −46.6 to −31.3‰), diagnostic of a biogeochemical methane cycle or acetogenesis, in shale and sandstone deposited in ~3 billion-years-old acidic volcanic lakes on the Kaapvaal Craton of southern Africa. A distinctive Al-rich mineral assemblage with abundant pyrophyllite in lacustrine sedimentary rocks bears similarity to modern volcanic rocks affected by circulation of hot acidic fluids. This is compounded with an enrichment of Ni, Mo, W, As and Cu in whole-rock analyses of sedimentary rocks, which is also observed in geothermal areas of modern volcanic environments. Analysis of early diagenetic pyrite in these sedimentary rocks indicates high nutrient level in the lake, which might reflect hydrothermal input with leaching of volcanic material. Despite the restricted and ephemeral nature of volcanic lakes, a highly productive and complex ecosystem established itself in this environment. Volcanic lakes during the Mesoarchaean thus served as an ecological niche for the development and diversification of microbial life on emerged continental landmasses.

1. Introduction

Following the large-scale emergence of continental landmasses in the later part of the Archaean, ~3 to 2.5 billion years ago (Bindeman et al., 2018), life established itself on land. In order to colonise this new frontier, life would have had to diversify and adapt to a landscape characterised by intense UV radiation, wetting-drying cycles, and a greater variability in temperature, salinity, light exposure and availability of nutrients and bioessential trace metals, such as S, P, Fe, Mo and Zn in comparison to marine environments (Beraldi-Campesi, 2013; Flannery et al., 2016; Stüeken and Buick, 2018).

When this process of land colonisation started, and how fast and under what conditions it developed is poorly constrained due to the scarcity of non-marine Archaean deposits. Examples of early life in purportedly non-marine environments include freshwater stromatolites in lacustrine sediments (Awramik and Buchheim, 2009) and traces of endolithic organisms in fluvial sediments of the ~2.7 Ga Fortescue Group of Western Australia (Rasmussen et al., 2009), evidence for methanogens, photoautotrophs and sulfate reducers in the 2.9–2.8 Ga Witwatersrand Supergroup of South Africa (Guy et al., 2012; Mossman et al., 2008) and traces of methanogens in the 3.0 Ga Lalla Rookh Sandstone, Western Australia (Stüeken and Buick, 2018). Isotopic and microtextural evidence for even older life forms has also been claimed from clastic sedimentary rocks of the 3.2 Ga Moodies Group, South Africa (Homann et al., 2018; Nabhan et al., 2016) and sinter deposits of the 3.48 Ga Dresser Formation, Western Australia (Djokic et al., 2017). In fact, some workers have proposed that life may have developed on land, and only later adapted to marine conditions (Beraldi-Campesi, 2013; Mulkidjanian et al., 2012).

In this study, we present geological and geochemical data for a little-known occurrence of carbonaceous shales within the dominantly volcanic intracratonic succession of the Dominion Group, South Africa. Geological and sedimentological criteria favour a non-marine depositional environment for the shales, and mineralogical and whole-rock geochemical data constrain the sediment source

* Corresponding author at: Department of Earth Resource Science, Akita University, Akita 010-8502, Japan.
E-mail address: andrea.agangi@gmail.com (A. Agangi).

https://doi.org/10.1016/j.epsl.2020.116725

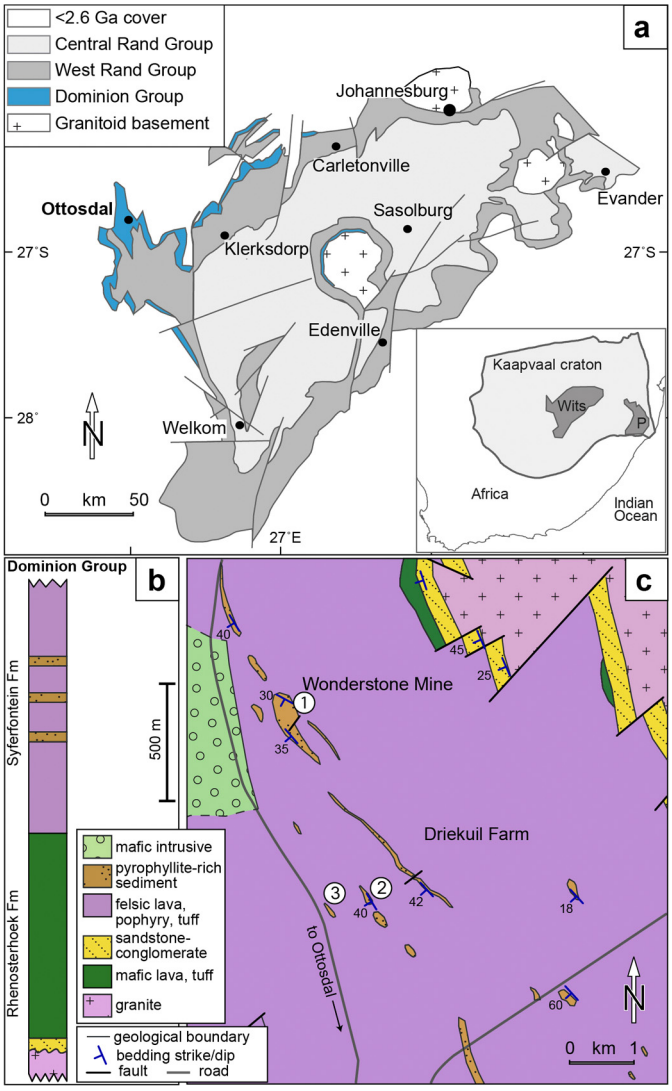

Fig. 1. Geological map and stratigraphic column of the Dominion Group in the study area. **a**, Geological map of the Witwatersrand basin (Dominion Group indicated in blue) and location on the Kaapvaal Craton (inset). Wits: Witwatersrand Supergroup, P: Pongola Supergroup. **b**, Stratigraphic column of the Dominion Group in the area surrounding the town of Ottosdal (after Jackson, 1992). **c**, Geological map of the area north of Ottosdal (after Nel et al., 1937). (For interpretation of the colours in the figure(s), the reader is referred to the web version of this article.)

and alteration conditions. Further, we use C-isotope composition of the carbonaceous matter to constrain the possible metabolic processes that operated in this early terrestrial environment.

2. Geological setting

The intracontinental sedimentary rocks deposited on the Kaapvaal Craton of southern Africa from around 3.1 Ga represent a well-exposed archive to study terrestrial surface processes operating on one of the earliest landmasses following its large-scale emergence. In this study, we present evidence for life colonisation of restricted, intracratonic basins interpreted to be volcanic lakes. Failed rift basins in the central Kaapvaal Craton accommodated the Dominion Group (Fig. 1a, b), a volcano-sedimentary succession that rests over an extensive nonconformity that represents craton-scale emergence and subsequent peneplanation on a >3.1 Ga basement (Jackson, 1992). Subaerial exposure is demonstrated by the volcanic facies (massive amygdaloidal lavas lacking pillow structures, presence of high-temperature rheomorphic tuffs), and by palaeosols developed at the contact with the basement granites (Grandstaff et al., 1986) and in mafic lavas of the Rhenoesterhoek Formation (Crow and Condie, 1987). The Dominion Group is up to 2700 m in thickness and commences with a thin veneer of sandstone and conglomerate above the nonconformity that is interpreted to have been deposited in a fluvial setting. The bulk of the succession is dominated by massive, amygdaloidal mafic to intermediate lavas with no reported pillow structures, felsic porphyry and ignimbrites interpreted to have been deposited largely in a subaerial environment (Agangi et al., 2020; Jackson, 1992; Wang et al., 2020). Available U–Pb zircon ages for felsic volcanic rocks (3074 ±6 Ma; SHRIMP analyses; Armstrong et al., 1991) and basement granite (as young as 3101 ±2 Ma; ID-TIMS analyses; Robb and Meyer, 1995) suggest a relatively rapid cycle of granite intrusion, uplift, erosion and subsequent volcanism. Interbedded with the volcanic rocks are thin (tens of metres in thickness) packages of water-lain sedimentary rocks (shale and minor sandstone) locally known as wonderstone and mined for their high pyrophyllite content. Their abundant carbonaceous matter reveals evidence for biomass production in a volcanically dominated terrestrial environment ~3.0 Ga ago.

3. Results

3.1. Field characteristics of shales and volcanic rocks of the Dominion Group

We studied three localities north of Ottosdal, where sedimentary rocks intercalated with felsic volcanic rocks crop out discontinuously for a total length of several km along strike (Fig. 1c): Wonderstone Mine (locality 1), an abandoned quarry on Driekuil Farm (locality 2), and a thin sedimentary lens nearby (locality 3). Fresh outcrops occur in quarries in an otherwise flat, mature landscape. The sedimentary succession dips at an average angle of 35° towards the SW and consists largely of interbedded carbonaceous and variably pyrite-rich shale and arenite intercalated with felsic volcanic rocks.

At Wonderstone Mine, the contact between volcanic and overlying sedimentary rocks is locally tectonised. Where underformed, the volcanic rocks are overlain by a 3–6 m-thick organic carbon-lean sandstone with trough-cross bedding and ripple laminations. This unit is composed of coarse-grained pebbly sandstone at the base and fines upwards to medium-grained sandstone. Over a circa 1 m interval, the sandstone becomes carbonaceous and grades into a carbonaceous shale. The latter is composed of a thick succession of thickly bedded, but mostly massive shale intercalated with lithic arenite (Fig. 2a). Their grey to black colour is indicative of variable carbon content. Locally, a discolouration of the shale was observed close to the surface, suggesting that long-term, recent weathering affected the carbon content of these rocks. Decimetre-scale, graded beds of arenite with erosional base topped by thinly laminated shale are locally well exposed (Fig. 2b).

We interpret the graded arenite beds as lacustrine turbidites (cf. Bouma, 1962) and intervening shales as 'background' suspension deposits. Abundant pyrite occurs as finely disseminated grains and cm-size nodules and layers at multiple horizons at localities 1 and 2 (Fig. 3a, Fig. 4). Besides planar stratification and normal grading, rare wave-generated ripple marks with sinuous crests were observed at Wonderstone Mine (Fig. 2c). Overall, the succession reflects flooding of the volcanic substrate and deepening of the sedimentary succession, as demonstrated by the upwards fining pattern.

Volcanic rocks enclosing the sedimentary rocks include massive-textured to flow-banded feldspar-quartz-phyric felsic lavas and foliated volcanic deposits, which may represent rheomorphic ignimbrites or flow-folded lavas (Fig. 3c, 3d). Above the upper contact

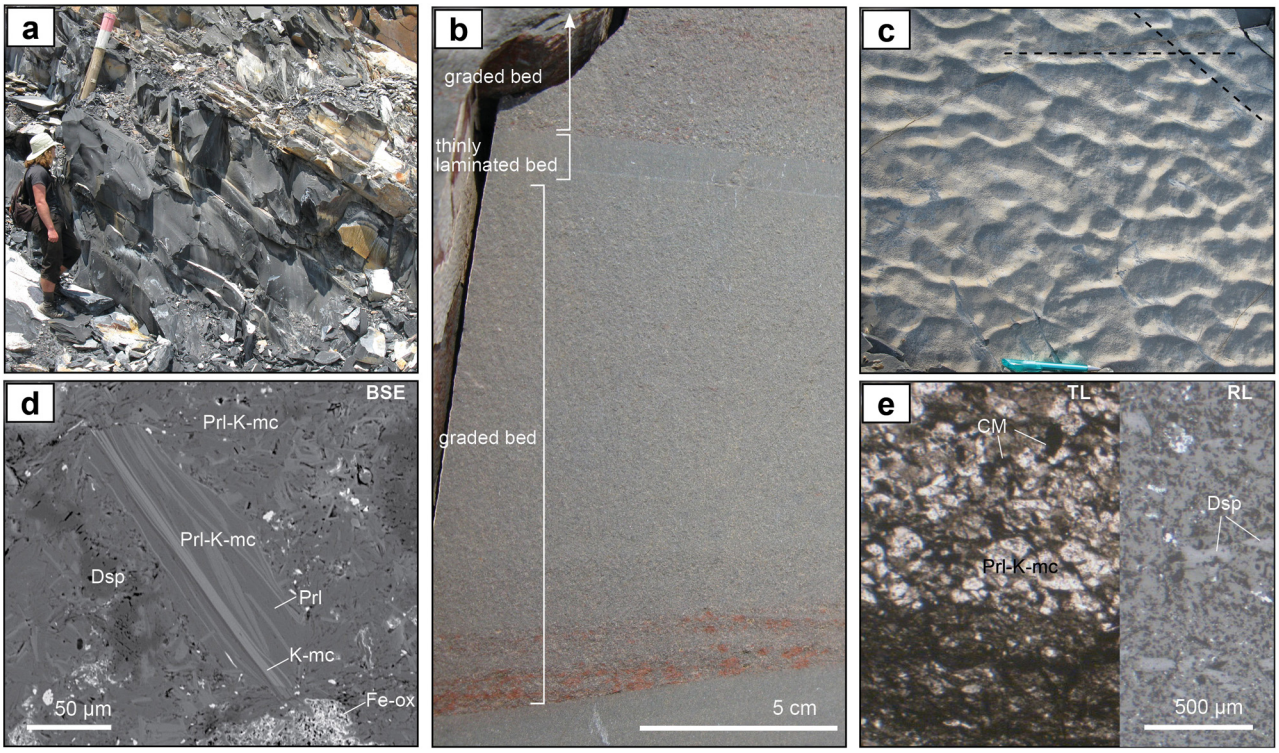

Fig. 2. Field and microtextural characteristics of studied rocks. **a**, Thickly bedded carbonaceous shales at Wonderstone Mine (locality 1, S26°44′4.03″ E025°59′50.07″). **b**, Graded sandstone-siltstone bed (Bouma Ta interval) overlain by a thin layer of finely laminated siltstone (Te; locality 2, Driekuil Farm, S26°45.571′ E026°02.590′). The beds are part of a sequence of alternating graded sandstone and thinly laminated shale. **c**, Sinuous interference ripple marks in shale at locality 1. Dashed lines at the top of the figure indicate main crest orientations. **d**, Grain of interlayered pyrophyllite and K-mica (Prl-K-mc, centre) of possible detrital origin in a matrix composed of randomly oriented (secondary) pyrophyllite, K-mica, diaspore (Dsp) and Fe-oxide in graded sandstone, locality 2 (SEM-BSE image). **e**, Contact between carbonaceous shale (bottom of image) and fine-grained sandstone (top) containing grains of pyrophyllite-K-mica and secondary diaspore. In the sandstone layer, carbonaceous matter (CM) occurs within irregular clasts, suggesting reworking, as well as finely dispersed in pyrophyllite, locality 1 (optical microscope image, left – plane polarised transmitted light, right – reflected light).

of the sedimentary rocks, mudstone clasts were observed in the overlying flow-foliated volcanic rocks (Fig. 3b). Spherulite-textured feldspar-phyric igneous rocks were also found within the sedimentary rocks at Wonderstone Mine.

3.2. Alteration of sedimentary and volcanic rocks

The sedimentary rocks are primarily composed of pyrophyllite, white K-mica (likely muscovite), pyrite, rutile and carbonaceous matter (Fig. 2d, e). Primary detrital minerals and early alteration assemblages have been overgrown by aggregates of randomly oriented diaspore grains (Fig. 2e). Carbonate is consistently absent from all sedimentary samples. Accessory minerals include rare earth element (REE)-bearing Al-phosphate minerals and tourmaline. Pyrophyllite forms grains with contrasting textures, which suggest multiple generations. Randomly oriented pyrophyllite crystals less than 50 µm in size (Fig. 2d) are likely secondary. This type of pyrophyllite is finely intergrown with carbon (see detailed description below). In addition, slightly larger pyrophyllite grains (100–200 µm in size) with round habit, interlayered with K-mica (Fig. 2d) and free of organic matter, might have a detrital origin. Pyrophyllite also occurs in pressure shadows around pyrite as elongate crystals oriented parallel to the direction of extension, suggesting that pyrophyllite also formed during sediment compaction and diagenesis (Fig. 3e).

The felsic volcanic rocks show two contrasting alteration assemblages: 1) a chlorite-carbonate-K-mica assemblage providing a green colour, or brown in weathered samples, which is indistinguishable from the regional metamorphic assemblage (Agangi et al., 2020; Jackson, 1992); and 2) a pyrophyllite-K-mica-quartz-rutile assemblage observed in white to pale grey, "bleached" samples. Samples affected by the former alteration retain magmatic apatite and Fe-oxide (magnetite), whereas those affected by the latter alteration contain, similar to the sedimentary rocks, aggregates of fine-grained REE-bearing Al-phosphate minerals and rutile instead of magmatic apatite and magnetite. At localities 1 and 3, the distribution of alteration products in volcanic rocks is asymmetric with respect to the sedimentary rocks, with the most intensely altered, pyrophyllite-K-mica-rich and bleached rocks observed immediately underneath the sedimentary rocks, and chlorite-bearing assemblages observed immediately stratigraphically above the sedimentary rocks. This asymmetric distribution of alteration products, which is clearly visible in drone images for locality 3 (Fig. 4b), is consistent with a syn-genetic, pre- to syn-depositional pyrophyllite alteration in volcanic rocks.

Bulk-rock chemical analyses indicate that, in comparison with the least-altered felsic volcanic rocks, the sedimentary rocks have very high Al_2O_3 and TiO_2 contents and loss on ignition (30.2–35.8 wt%, 1.6–1.9 wt% and 5.8–7.7 wt%, respectively), and are moderately to strongly depleted in Na_2O, K_2O, CaO, Fe_2O_3, P_2O_5, Ba and Zn (Fig. 4a, 4b, Supplementary Table 1). In an Al_2O_3 – $10\times(Na_2O+K_2O)$ – $10\times(TiO_2)$ plot (Fig. 4a), the samples form a linear trend with nearly constant Al_2O_3/TiO_2 ratio and decreasing alkali content in progressively more altered samples. In a $CaO+Na_2O+K_2O$ – Al_2O_3 – $FeO+MgO$ plot (Fig. 5b), chlorite-bearing felsic volcanic samples form a trend away from the $CaO+Na_2O+K_2O$ apex, whereas the bleached volcanic samples and the sedimentary rocks plot closer to the Al_2O_3 apex. Volcanic samples have fractionated primitive mantle-normalised rare-earth element patterns, with moderately negative Eu anomalies ($Eu/Eu^* = 0.6 – 0.7$, Fig. 5c). The sedimentary rocks also have fractionated LREE–HREE patterns that overall match those of felsic volcanic

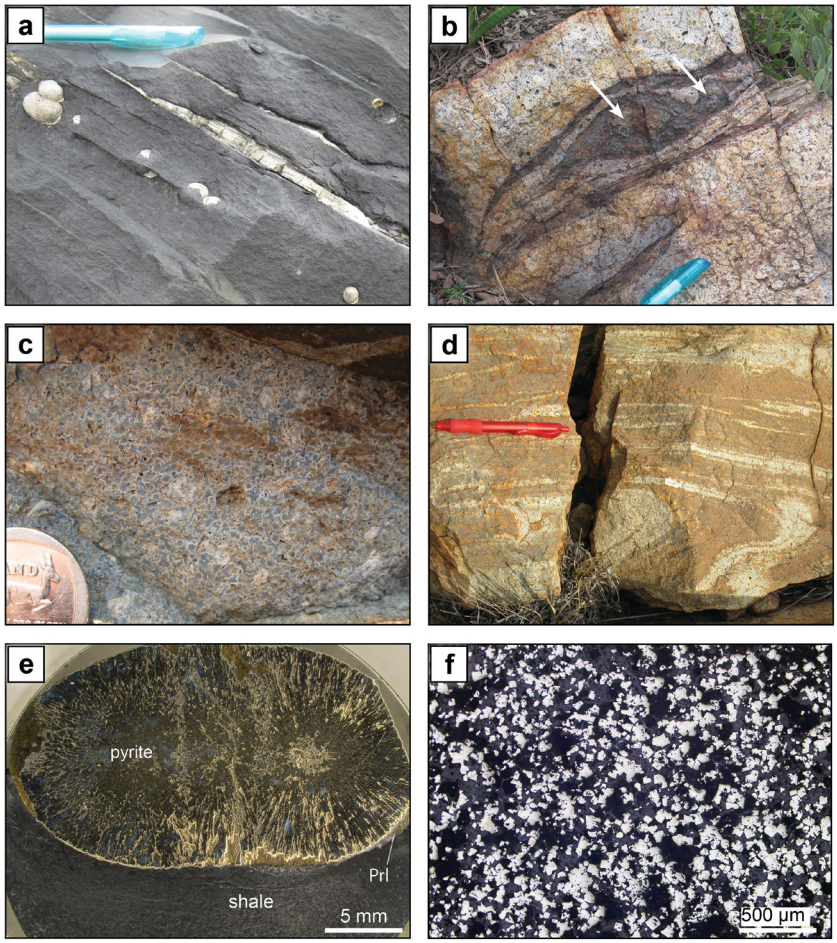

Fig. 3. Textures of sedimentary and volcanic rocks of the Dominion Group in the Ottosdal area. **a**, Laminated black shale containing pyrite nodules and layers (locality 1, Wonderstone Mine). **b**, Centimetre-scale angular clasts of mudstone (indicated by arrows) in flow-banded volcanic rock at Wonderstone Mine, locality 1. **c**, Feldspar-phyric, spherulitic-textured lava, and **d**, Flow-banded and folded volcanic rock, locality 3. **e**, Diagenetic pyrite nodule in carbonaceous shale and pyrophyllite (Prl) growing in a pressure shadow (shale sample DWS49, Wonderstone Mine, locality 1). **f**, Fine-grained, semi-massive pyrite in shale (sample DWS6K, Wonderstone Mine, locality 1).

rocks, but have variably depleted REE concentrations in comparison to volcanic samples. Volcanic and sedimentary rocks have strongly contrasting base-metal concentrations; for example, Ni, W, As, Mo and Cu are moderately to strongly enriched in the sedimentary rocks compared to the least-altered volcanic rocks (Fig. 5d). In contrast, bleached volcanic rocks are depleted in all these elements (Fig. 5e). Other metals, such as Cr and V, are enriched in the sedimentary samples in comparison with the felsic volcanic samples. Chromium and V are expected to behave conservatively under reducing conditions (as Cr^{3+} and V^{3+}), and to become mobile under oxidising conditions (as Cr^{6+} and V^{5+}). Thus, Cr/Nb and V/Nb can be used to estimate relative contribution from mafic and felsic sources, under the assumption that these metals behaved conservatively during alteration in a low-oxygen surface conditions expected for the Mesoarchaean. In a plot of V/Nb vs Cr/Nb, the sedimentary rocks have intermediate composition between the felsic volcanic rocks and the average composition of the Dominion Group mafic volcanic rocks from the Klerksdorp area (Agangi et al., 2020) (Fig. 5f). Bleached volcanic rocks have lower Cr/Nb and V/Nb in comparison to the least altered felsic volcanic rocks.

Collectively, these observations suggest sediment derivation from the associated volcanic rocks of the Dominion Group. The elevated Cr and V concentrations and Cr/Nb ratios relatively to felsic rocks are compatible with some contribution from mafic volcanic sources, and a two-component mixing model suggests contribution of as much as approximately 20% of mafic rocks. However, this estimate assumes an immobile behaviour of Cr and V during alteration, and should be considered as a maximum value, especially in view of evidence for mobility of Cr^{3+} under acidic conditions (Konhauser et al., 2011). Leaching of major and trace elements (e.g. alkalis, Ca, Fe, Zn and Rb) from bleached volcanic and sedimentary rocks in association with hydration, and residual enrichment in the most "fluid-immobile" elements, such as Al, Ti, Nb and Zr indicates removal of fluid-soluble elements during intense alteration. The sedimentary rocks may have acquired such geochemical signature either through alteration of fresh volcanic-derived material or through erosion of already altered volcanic rocks similar to the bleached volcanic rocks, or both. The enrichment in some mobile elements (e.g. Ni, W, As and Mo) far exceeds the enrichment in immobile elements and implies net gain of these elements to the sedimentary rocks during alteration processes (Fig. 5d).

3.3. Carbonaceous matter, total S, organic C contents and C isotopes

Petrographic observations reveal that carbonaceous matter occurs as: 1) thin strands and flakes between pyrophyllite grains in shales; and 2) within irregular clasts in arenites (Fig. 2e, Fig. 6). These observations suggest a detrital origin of the second type of organic matter, which is consistent with erosion of carbonaceous sediment by turbidity current and incorporation into the graded sandstone beds as clasts. Overall, the shale samples appear darker (richer in C) than the arenites, although mm- to cm-scale alternating shale laminae with variable C-content are present in some samples (see TOC data below). In addition, Raman spectroscopy

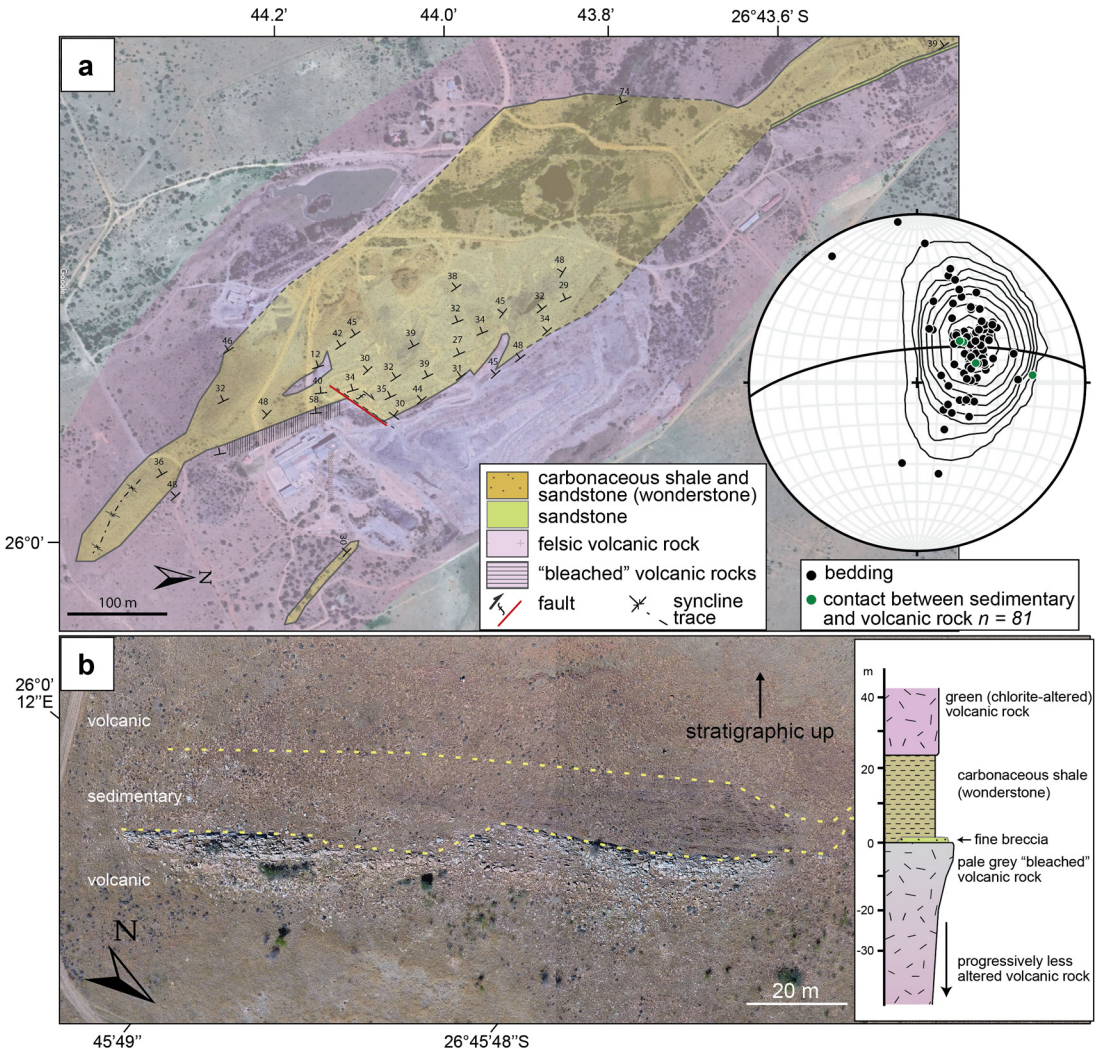

Fig. 4. a. Simplified geological map of the Wonderstone Mine (Locality 1) and stereoplot (lower hemisphere) of poles of bedding planes and contacts between sedimentary and volcanic rocks. Contours outline the density distribution of poles. **b.** Composite drone image at Locality 3, showing a thin lens of carbonaceous shale, the underlying intensely altered "bleached" volcanic rocks and the overlying brown-weathering chlorite-altered volcanic rocks. The Inset shows a simplified stratigraphic log.

maps show that carbonaceous matter is finely dispersed in randomly oriented fine-grained pyrophyllite and K-mica (Fig. 6). Raman spectra of carbonaceous matter have well-developed peaks at 1350 and 1605 cm^{-1}, typical of disordered C (Sforna et al., 2014). Whole-rock analysis of 16 samples of carbonaceous shale and arenite from Wonderstone Mine and Driekuil Farm indicates that they contain 0.1 to 1.5 wt% total organic carbon (TOC). The $\delta^{13}C_{org}$ values range between −46.6 and −34.3‰ with a prominent peak centred at ~-44‰ and three analyses forming a possible secondary peak at −35‰ in the frequency histogram (Fig. 7), and are broadly negatively correlated with TOC (Fig. 8a, Table 1).

Some samples with low TOC content were collected near the modern land surface, and thus conceivably lost some organic matter due to modern oxidative weathering. However, this process alone cannot account for near-to-10‰ fractionation of C isotopes (Petsch, 2014). In contrast, organic matter production in the modern weathering profile could result in enrichment of ^{13}C up to around 5‰ (Petsch, 2014). To test this possibility, we analysed separate layers in samples that contain both light and dark-coloured bands. One sample has dramatically different TOC contents and $\delta^{13}C_{org}$ values with light bands showing ^{13}C enrichment. The other sample has both bands with similar and relatively high TOC and similarly light $\delta^{13}C_{org}$ values (Fig. 8a). These observations are best

Table 1
Total organic C, total S and C isotope analyses of shales of the Dominion Group.

Sample	Note	TOC (wt%)	TS (wt%)	$\delta^{13}C_{org}$ (‰, VPDB)
DWS3	bulk	0.8	<0.01	−42.6
DWS6A	bulk	1.5	0.10	−44.4
DWS7	bulk	1.2	<0.01	−42.7
DWS1	bulk	0.1	<0.01	−34.3
DWS5	bulk	0.1	<0.01	−35.9
DWS17A	bulk	0.5	0.07	−41.0
DWS24	bulk	0.2	0.23	−39.0
DWS29C	bulk	0.2	<0.01	−36.0
DWS35	bulk	0.9	0.10	−44.4
DWS38	bulk	0.7	0.39	−45.4
DWS41	bulk	0.7	0.02	−43.8
DWS48	bulk	1.0	0.02	−42.9
DWS49	bulk	0.7	0.08	−46.6
DWS50	bulk	0.6	0.02	−43.4
DWS64	bulk	0.9	0.53	−46.4
DWS65	bulk	0.8	<0.01	−40.2
DWS29BC	split	0.1	1.49	−31.2
DWS29BF	split	0.4	1.30	−43.6
DWS30C	split	0.7	0.01	−44.2
DWS30F	split	1.0	0.02	−44.1

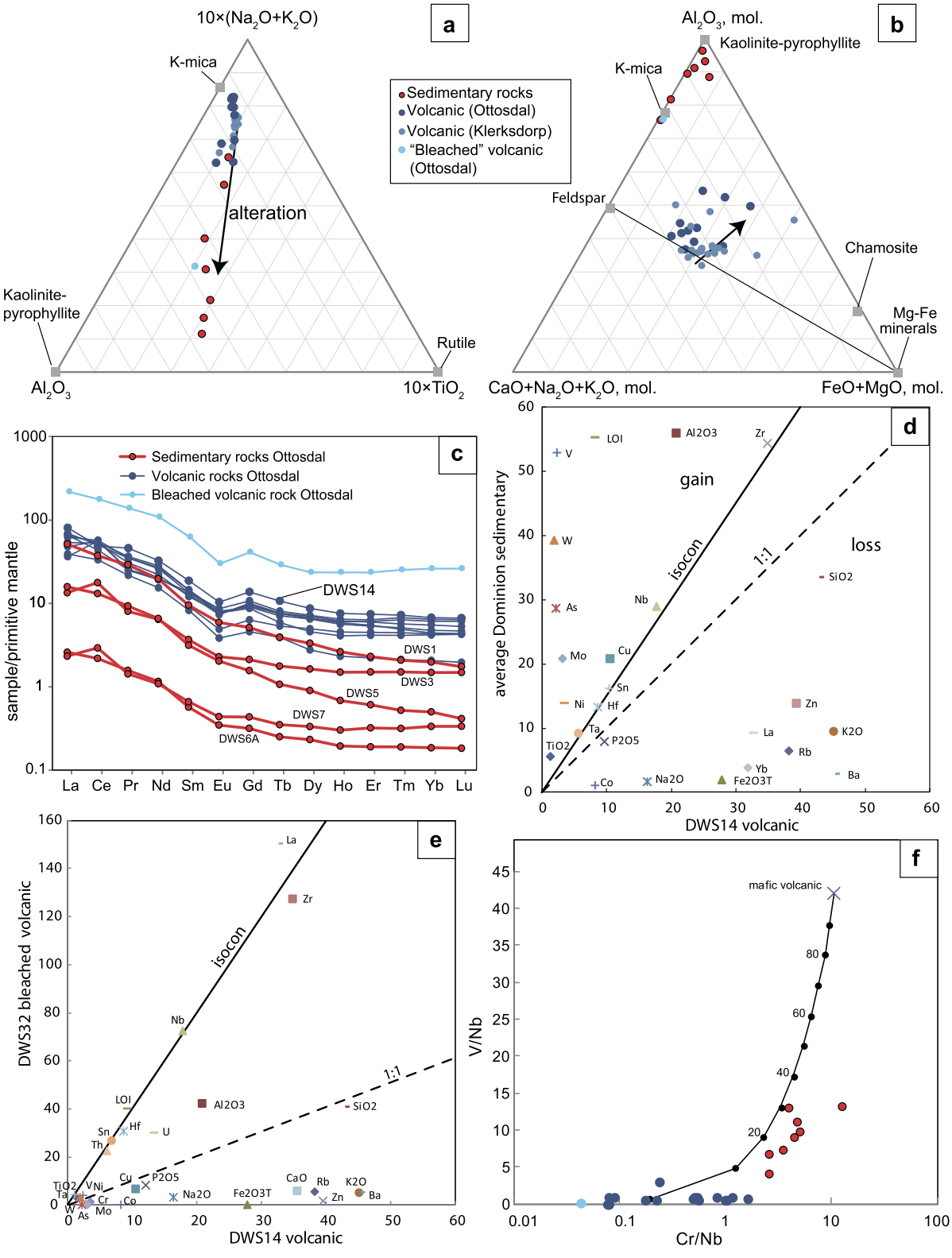

Fig. 5. Major and trace element composition of sedimentary and volcanic rocks of the Dominion Group. **a**, Plot of Al_2O_3 – 10×(Na_2O+K_2O) – 10×TiO_2; all concentrations are in weight per cent. **b**, Plot of CaO+Na_2O+K_2O – Al_2O_3 – FeO+MgO in molar proportions. Arrows in A and B indicate direction of increasing alteration. Volcanic rocks from the Ottosdal and Klerksdorp areas are compared. **c**, Primitive mantle-normalised rare earth element data. **d**, Isocon diagram for the average sedimentary rock in the Ottosdal area (on the y-axis) compared with the least-altered volcanic rock (sample DWS14, x-axis) showing enrichment in elements such as V, W, As and Mo, and depletion of alkalis, Fe and Ba. The isocon line connects the most fluid-immobile elements, such as Ta, Nb, Zr and Hf. **e**, Isocon diagram for the bleached volcanic rocks (sample DWS32). **f**, Mixing model of felsic and mafic volcanic rocks of the Dominion Group (mafic volcanic rocks from Agangi et al., 2020).

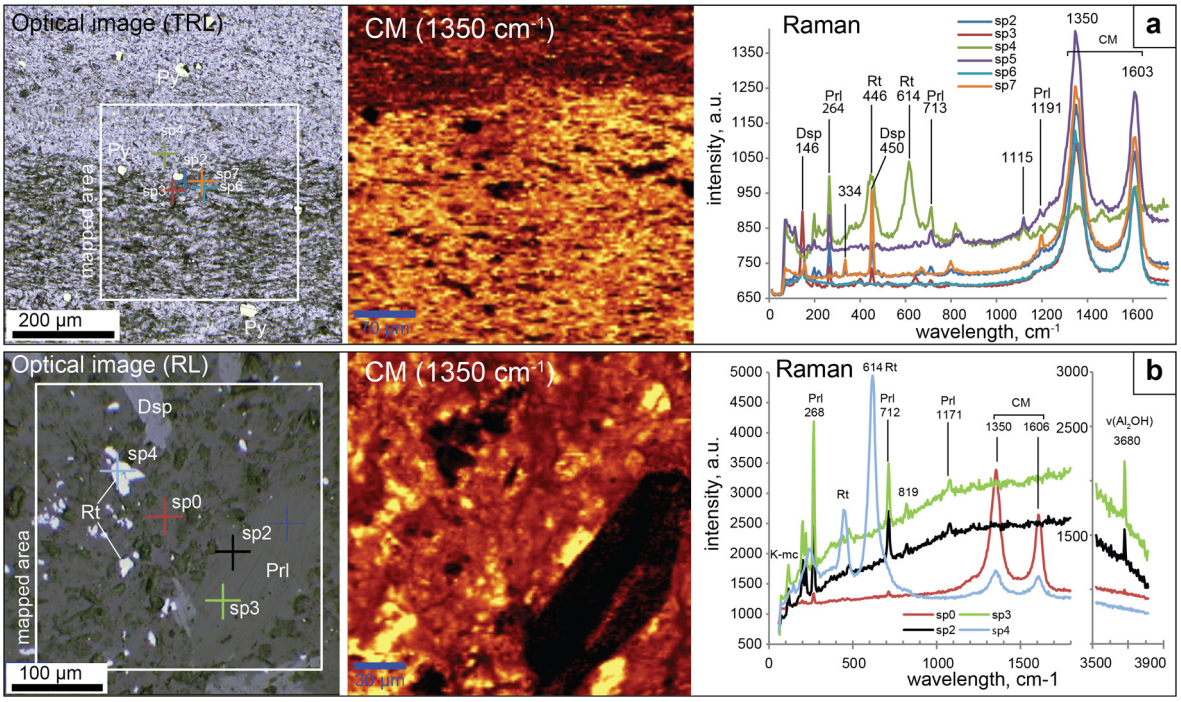

Fig. 6. Optical images, Raman maps and spectra of carbonaceous sedimentary rocks from the Dominion Group. **a**, Contact between carbon-rich and carbon-poor layers (sample DWS29B, Wonderstone Mine). **b**, Round, C-poor grain of pyrophyllite (bottom right) surrounded by C-bearing fine-grained pyrophyllite (sample DWS6, Wonderstone Mine). CM carbonaceous matter, K-mc white K-mica, Py pyrite, Dsp diaspore, Prl pyrophyllite, Rt rutile, RL reflected light, TRL transmitted and reflected light.

explained by low TOC bands and samples reflecting primary productivity with relative ^{13}C enrichment, whereas darker bands reflect sufficient burial of C_{org} derived from primary productivity to fuel secondary productivity (methanogenesis and methanotrophy or acetogenesis) (Karhu and Bekker, 2020). We thus infer that while organic matter could have experienced significant loss through oxidative weathering in the modern weathering profile, $\delta^{13}C_{org}$ values still largely reflect primary depositional signal. Total S content of whole-rock samples spans from below the detection limit (<0.01 wt%) to around 0.5 wt% and, similarly to TOC content, shows a broad negative correlation with $\delta^{13}C_{org}$ values (Fig. 8b); individual layers in one sample yielded TS content up to 1.5 wt%.

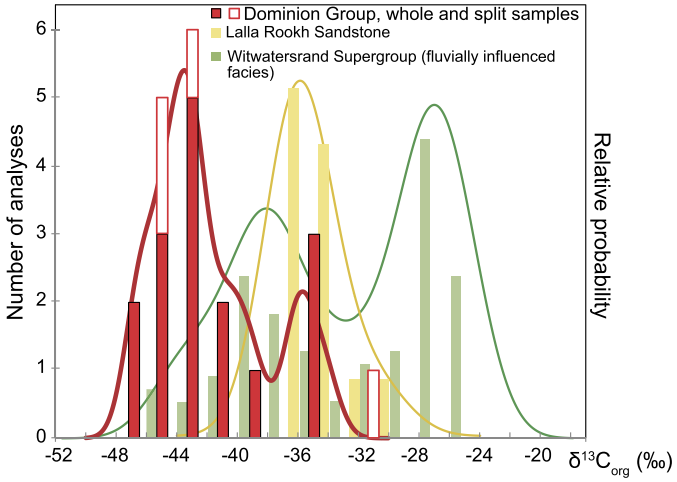

Fig. 7. C isotope compositions of the Dominion Group sedimentary rocks. Data for the Dominion Group are shown for whole-rock samples (solid red) and discrete layers (split sample, unfilled red).

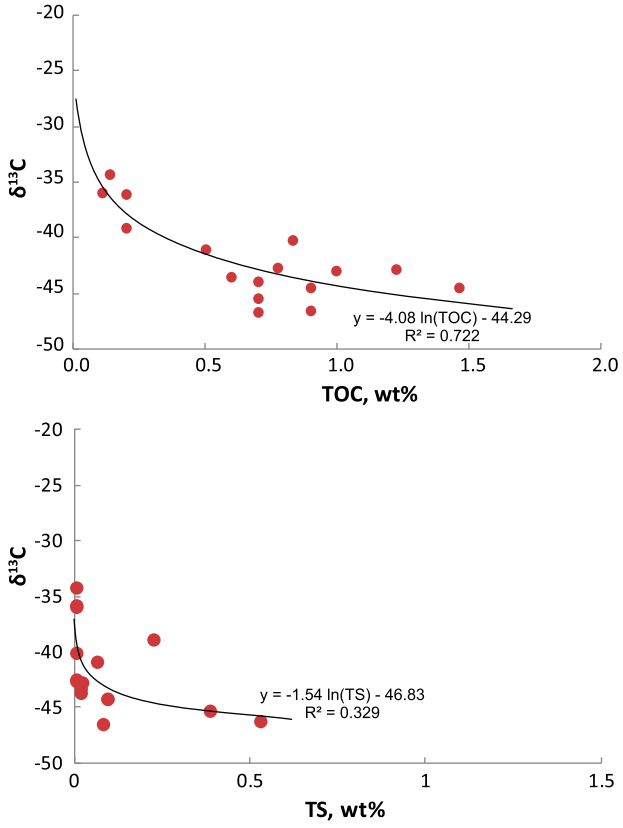

Fig. 8. Plot of C isotope values versus total organic carbon content ($\delta^{13}C$ vs TOC) **(a)** and C isotope values versus total S content ($\delta^{13}C$ vs TS) **(b)** of the Dominion Group sedimentary rocks. The black lines represent the logarithmic best fit for whole-rock analyses; analyses of split samples are connected by dashed lines.

3.4. Trace element content of pyrite

The trace-element composition of diagenetic pyrite measured in situ by laser ablation ICP-MS is used as a first-order proxy for the trace-metal availability during sedimentation and early diagenesis of the Dominion Group sediments and, ultimately, the influx of metals to the basin (cf. Mukherjee and Large, 2017). The latter may have been controlled by various processes, including hydrothermal input (from direct magmatic degassing and rock alteration), surface weathering of fresh volcanic material and detrital transport.

The analysed pyrite has two main textures: 1) spherical, cm-size nodules with inclusion-rich cores and radial crystalline rims, and 2) μm-size, disseminated to semi-massive pyrite (Fig. 3a, 3e, 3f). Inclusions of pyrophyllite and chalcopyrite have been identified in nodule cores. The radial textures with spearhead twins are reminiscent of marcasite (Schieber, 2007), and suggest inversion to pyrite during burial diagenesis and metamorphism. Marcasite formation is favoured at low pH and is typical of epithermal environments and coal deposits (Schoonen and Barnes, 1991). Marcasite is unstable, and tends to invert to pyrite during post-sedimentary processes (Schieber, 2007). The Dominion Group pyrites have higher average concentrations of Zn (54 ppm), Ag (82 ppm), Sb (443 ppm), Se (34 ppm) and Co (2480 ppm), and have similar concentrations of Mn (16 ppm), Mo (5.2 ppm) and As (1080 ppm) compared to pyrite from carbonaceous marine shales of similar (Mesoarchaean) age (Supplementary Fig. 1, Supplementary Table 2). The Cu concentrations are somewhat lower than the maximum values in pyrite from marine shales, but the presence of chalcopyrite inclusions in our pyrite samples implies additional Cu that was not accounted for in our LA-ICP-MS analyses, as inclusions were intentionally avoided during the analysis.

4. Discussion

4.1. Conditions of sedimentation and alteration in a volcanic environment

Distinguishing between shallow-marine and non-marine depositional environments in ancient sedimentary successions is typically challenging, as reflected for example by the long-lasting discussion on the Tumbiana Formation of the Fortescue Group, Western Australia (Awramik and Buchheim, 2009; Sakurai et al., 2005). For these rocks, various sedimentological and geochemical criteria have been proposed to constrain the depositional environment of shallow water stromatolites (Awramik and Buchheim, 2009; Bolhar and Van Kranendonk, 2007). Perhaps the strongest argument for a non-marine setting, which also applies to the sedimentary rocks of the Dominion Group described in this study, is based on the fact that the sedimentary rocks are sandwiched between subaerially emplaced volcanic rocks and the proximity of fluvial sedimentary rocks (Buick, 1992).

Our field observations indicate that the Dominion Group sedimentary rocks in the Ottosdal area were deposited in an active volcanic setting that was subjected to subaqueous deposition of fine-grained volcanic-derived sediment by turbidity currents. Lake turbidites are also known from large modern lacustrine systems and are controlled by atmospheric and volcanic processes, such as storms, volcanic eruptions and earthquakes (Moernaut and De Batist, 2011; Shiki et al., 2000). The mostly sub-wave base nature of the sediment and lack of facies variations both vertically over tens of metres and laterally over several kilometres suggests deposition in km-scale lakes. These lakes occupied depressions, and remained underfilled with sediments in the course of most of their life span, being subjected episodically to events of lake-bottom sediment reworking, as indicated by rare wave ripples.

The stratigraphic abundance and lateral extent of low-pH minerals, such as pyrophyllite and marcasite, and the absence of carbonate, suggest that acidic conditions persisted during sedimentation and early diagenesis. At such low pH conditions, magmatic apatite is dissolved, as shown by its absence in “bleached” volcanic and sedimentary rocks, thus liberating phosphorus into the hydrothermal fluids (Hedenquist and Lowenstern, 1994) and delivering it to the lakes, where it could have been utilised as an important nutrient (Brasier, 2014). In addition, the presence of tourmaline in the sediments implies the availability of boron in the basin, potentially related to the supply with hydrothermal fluids.

Interpretation of such alteration requires taking into consideration the volcanic setting, as well as the atmospheric conditions expected in Archaean environments, with two mechanisms envisaged. On the one hand, the high degree of alteration and the development of high-Al minerals are typical of acid leach alteration observed in intermediate- to high-sulfidation epithermal environments (Supplementary Fig. 2a) (Arribas, 1995). The clear asymmetric distribution of alteration assemblages with respect to sedimentary rocks with strongly “bleached” volcanic rocks underneath sedimentary rocks (Fig. 4b) constrains low-temperature, hydrothermal alteration to a pre- to syn-sedimentation stage. The enrichment in base metals (i.e., Ni, Mo, V, and As) such as in the sedimentary rocks is typically observed around hydrothermal pools formed in active geothermal areas, such as New Zealand and the Yellowstone Park of the Western US (Weissberg, 1969). On the other hand, leaching of Fe has been reported from volcanic rocks of the Neoarchaean Fortescue Group, Western Australia, where it has been interpreted to reflect weathering under a high-CO_2, anoxic atmosphere, favouring low-pH conditions and preventing formation of insoluble Fe(III)-oxides (Macfarlane et al., 1994), possibly combined with post-depositional alteration (Teitler et al., 2015). However, it is commonly accepted that P was not efficiently released from Archaean paleosols, in contrast to the surface weathering conditions during the GEO, which were characterised by acidic groundwater and higher P mobility (Bekker and Holland, 2012). Apatite is preserved in altered zones of the Mt Roe paleosols together with pyrophyllite and diaspore (Teitler et al., 2015), although local P-depletions may be attributed to the presence of organic ligands (Neaman et al., 2005). These Archaean weathering horizons also contain high-Al minerals, such as pyrophyllite and diaspore (Macfarlane et al., 1994; Teitler et al., 2015). However, in these cases, base metal enrichment has not been observed in associated terrestrial sediments. We note that the two mechanisms (volcanic degassing-driven alteration and surface weathering) are not mutually exclusive, and may have operated in concert in a subaerial volcanically dominated setting.

In either case, the low-pH alteration that affected the sediments is consistent with deposition in a sedimentary basin separated from the ocean, since such acidic conditions would not persist in open-marine settings regarded to have had a near-neutral pH in the Archaean (Krissansen-Totton et al., 2018). This observation further strengthens the interpretation of deposition in a non-marine environment. Despite the likely large variability of pH and temperature, terrestrial volcanic environments are known for hosting different microbial life forms (Pirajno, 2020), and are interpreted to have harboured life in the distant geological past (Djokic et al., 2017).

A first-order estimate of the time span for deposition of these sediments could be inferred by considering typical sedimentation rates for similar modern environments. Using sedimentation rates of 0.95 to 3.8 m/ka estimated for modern volcanic lakes of the Ethiopian Rift Valley (Telford and Lamb, 1999; Tiercelin et al., 2008), deposition of tens of metres of sediments would have taken 10^4 to 10^5 years.

4.2. An environment capable of fostering life

The presence of carbonaceous matter with ^{13}C-depleted isotopic compositions, especially prominent between 2.8 and 2.6 Ga, has been interpreted as an indication of enhanced methane production and recycling in the later Archaean (Hayes, 1994) or acetogenesis (Slotznick and Fischer, 2016). Values of $\delta^{13}C_{org}$ showing a relatively narrow range with a peak around −36‰ measured in the ~3.0 Ga Lalla Rookh Sandstone (Fig. 7) have been interpreted to reflect a contribution from methanogenesis or acetogenesis (Stüeken and Buick, 2018). More scattered $\delta^{13}C_{org}$ values extending down to −44‰ found in fluvially influenced sandstone of the Witwatersrand Supergroup may reflect contribution of phototrophs, methanogens, anaerobic methanotrophs and sulfate reducers to the carbonaceous matter (Guy et al., 2012). Such low values of $\delta^{13}C_{org}$ in the mid to late Archaean rocks are especially common in terrestrial deposits or continentally influenced shallow marine deposits, suggesting a predominance of such metabolic processes in non-marine environments at that time (Flannery et al., 2016; Guy et al., 2012; Stüeken and Buick, 2018). In contrast, higher values of $\delta^{13}C_{org}$ around −34‰ in the ~2.7 Ga Tumbiana Formation stromatolites have been interpreted to be consistent with photosynthetic processes (Thomazo et al., 2009; see review in Lepot, 2020).

The two apparent modes in isotope composition of organic matter and C content measured for the Dominion Group sedimentary rocks suggest two styles of metabolic activity potentially driven by changes in the nutrient availability. Under normally dry conditions, nutrients released via acidic leaching were delivered to the basin and absorbed to clay minerals, whereas high rainfall would have released these nutrients from clays by neutralising basinal waters (Konhauser et al., 2019), resulting in higher productivity and burial of organic matter and subsequent expansion of methanogenic and, methanotrophic or acetogenic metabolisms.

Methanotrophy, which involves C-fixation through methane oxidation, may have occurred as either aerobic microbial assimilation of methane using O_2 produced by photosynthesis (Rye and Holland, 2000), or anaerobic oxidation of methane (AOM) using, as alternatives to oxygen, ferric iron, nitrate or sulfate as electron acceptors (Iversen and Jorgensen, 1985). Considering the abundance of pyrite in the sedimentary rocks, some of which shows sedimentary-diagenetic textures (Fig. 3) and the broad negative correlation between TS and $\delta^{13}C_{org}$ values (Supplementary Fig. 1b), AOM via sulfate reduction under anoxic to suboxic conditions could have contributed to C-fixation, similarly to what has been shown to operate in modern submarine settings via consortia of methanotrophic Archaea and sulfate-reducing bacteria (Boetius et al., 2000). Importantly, in a geothermally active environment, oxidised S-species can derive from degassing and disproportionation of volcanic SO_2, and the presence of sulfate would not require the presence of free oxygen in shallow water or the atmosphere. Furthermore, in such setting, acetogens could have efficiently utilised atmospheric, volcanic and hydrothermal carbon and hydrogen sources to synthesise acetate, which then could have been used as a food source by heterotrophs, including methanogens.

Organisms capable of methanogenesis belong to the Archaea domain (Douglas, 2009), and are known for their adaptation to high temperature and acidity. For example, in the strongly acidic crater lake Kawah Ijen, Indonesia (pH < 1), Archaea are the sole microorganisms present, whereas bacteria and eukarya were found in the moderately acidic waters (with pH up to 3.5) of river Banyupahit-Banyuputih that flows from the crater lake (Löhr et al., 2006). This zonation represents an example of microbial adaptation to varying pH and temperature conditions typical of these environments. Methanogens have also been observed in acidic volcanic lake Caviahue, Argentina with pH 2.6 (Koschorreck et al., 2008) and in river Rio Tinto, Spain, whose pH of 2.3 and high metal content are caused by oxidation of volcanic-hosted massive sulfide deposits by infiltrating meteoric waters (Amils et al., 2014). The unique features of cellular membranes of some Archaea belonging to the phylum Crenarchaeota, which have been proposed to provide protection from extreme temperature, pH and salinity (Zeng et al., 2018), might be shared by other archaea phyla such as Korarchaeaota and Marsarchaeota (Auchtung et al., 2011; Jay et al., 2018), which are found in acidic hot springs at Yellowstone National Park and in Kamchatka. Thus, despite potential differences between modern microorganisms living under an oxic atmosphere and their ancient counterparts from a predominantly anoxic world, volcanically dominated Archaean lacustrine depositional systems such as that of the Dominion Group may have harboured and favoured the development of a methane-cycling or acetogenic microbiota.

5. Conclusions

We conclude that the emergence of the first large continental masses during the Mesoarchaean created new environments that were swiftly colonised, even in potentially harsh conditions of low pH in a volcanic lake. This is demonstrated by the abundance of carbonaceous matter in lake sediments just a few tens of million years after the Kaapvaal Craton emerged as a continental landmass (Fig. 9). Modern subaerial volcanic environments are characterised by strong variations in solute concentrations, temperature and pH, as acidic hot-spring water mixes with meteoric water, giving rise to local conditions suited for diverse microorganisms (Koschorreck et al., 2008; Löhr et al., 2006), which is also expected for Archaean settings. The evidence presented here illustrates a microbial community that diversified and adapted to challenging conditions, and points to acidic volcanic lakes as viable ecological niches for life evolution on emerged land. Volcanism would have provided energy at thermal and chemical gradients, and acidic alteration would have released bioessential elements, including phosphate, sulfate, boron, and trace metals such as Zn, Mo, Se, Mn, Ni, Co and Cu (Kida et al., 2001; Schönheit et al., 1979). In addition, clay formed by rock alteration would have been a critical substrate for microbial colonisation (Mulkidjanian et al., 2012). Sedimentary successions that formed in this environment and experienced this type of alteration are typically prone to erosion and are rarely preserved in the Precambrian record, although they may have been extensive in subaerial settings on early continents during periods of intense volcanic activity (Harris et al., 2009).

In a similar way, acidic lake deposits on Mars that were formed during a volcanically active, wetter period of the history of the planet before 3.1 Ga ago may equally have harboured life (Eigenbrode et al., 2018). Modern terrestrial analogues have been proposed for early Mars (Cavalazzi et al., 2019), although Earth's presently oxygenated atmosphere makes any comparison spurious. Clay-rich volcanic lake deposits of the Dominion Group may represent a better terrestrial analogue for ancient Mars environments, and are suitable sites to study the emergence and evolution of life on land.

CRediT authorship contribution statement

Andrea Agangi: Conceptualization, Investigation, Methodology, Writing – original draft, Writing – review & editing. **Axel Hofmann:** Conceptualization, Funding acquisition, Supervision, Writing – review & editing. **Frantz Ossa Ossa:** Resources, Writing – review & editing. **Dóra Paprika:** Investigation, Writing – review & editing. **Andrey Bekker:** Conceptualization, Writing – review & editing.

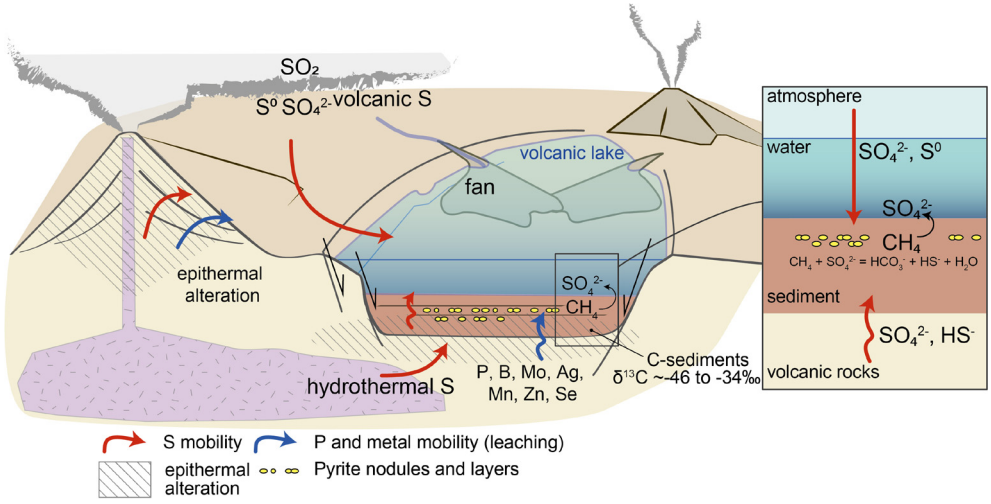

Fig. 9. Conceptual model for deposition in the Dominion Group volcanic lakes. Sedimentation occurred in an active volcanic setting, where degassing caused epithermal alteration and leaching of metals, boron and phosphorus from volcanic rocks. Delivery of these elements, together with S from various sources (as sulfate and sulfide) to the basin would have driven high productivity, including methanogenesis and methanotrophy and acetogenesis. Photochemical S-species derived from the atmosphere have also likely participated. Inset shows interaction between CH_4 and oxidising agents (e.g. sulfate) in the water column.

Declaration of competing interest

The authors declare that they have no known competing financial interests or personal relationships that could have appeared to influence the work reported in this paper.

Acknowledgements

This research was partly funded by CIMERA Centre of Excellence for Integrated Mineral and Energy Resource Analysis. We would like to thank Schalk Burger (Assore Ltd), John Tait, Charly Badenhorst, Rousseau du Toit and Phillip van der Bergh for access to mine properties and farmland.

Appendix A. Supplementary material

Supplementary material related to this article can be found online at https://doi.org/10.1016/j.epsl.2020.116725.

References

Agangi, A., Hofmann, A., Hegner, E., Xie, H., Teschner, C., Slabunov, A., Svetov, S.A., 2020. The Mesoarchaean Dominion Group and the onset of intracontinental volcanism on the Kaapvaal craton – geological, geochemical and temporal constraints. Gondwana Res. 84, 131–150.

Amils, R., Fernández-Remolar, D., the, I.T., 2014. Río Tinto: a geochemical and mineralogical terrestrial analogue of Mars. Life 4, 511–534.

Armstrong, R.A., Compston, W., Retief, E.A., Williams, I.S., Welke, H.J., 1991. Zircon ion microprobe studies bearing on the age and evolution of the Witwatersrand triad. Precambrian Res. 53, 243–266.

Arribas, A., 1995. Characteristics of high-sulfidation epithermal deposits, and their relation to magmatic fluids. In: Thompson, J.F.H. (Ed.), Magmas, Fluids, and Ore Deposits, pp. 419–454.

Auchtung, T.A., Shyndriayeva, G., Cavanaugh, C.M., 2011. 16S rRNA phylogenetic analysis and quantification of Korarchaeota indigenous to the hot springs of Kamchatka, Russia. Extremophiles 15, 105–116.

Awramik, S.M., Buchheim, H.P., 2009. A giant, Late Archean lake system: the Meentheena Member (Tumbiana Formation; Fortescue Group), Western Australia. Precambrian Res. 174, 215–240.

Bekker, A., Holland, H.D., 2012. Oxygen overshoot and recovery during the early Paleoproterozoic. Earth Planet. Sci. Lett. 317–318, 295–304.

Beraldi-Campesi, H., 2013. Early life on land and the first terrestrial ecosystems. Ecol. Process. 2, 1.

Bindeman, I.N., Zakharov, D.O., Palandri, J., Greber, N.D., Dauphas, N., Retallack, G.J., Hofmann, A., Lackey, J.S., Bekker, A., 2018. Rapid emergence of subaerial landmasses and onset of a modern hydrologic cycle 2.5 billion years ago. Nature 557, 545–548.

Boetius, A., Ravenschlag, K., Schubert, C.J., Rickert, D., Widdel, F., Gieseke, A., Amann, R., Jørgensen, B.B., Witte, U., Pfannkuche, O., 2000. A marine microbial consortium apparently mediating anaerobic oxidation of methane. Nature 407, 623–626.

Bolhar, R., Van Kranendonk, M.J., 2007. A non-marine depositional setting for the northern Fortescue Group, Pilbara Craton, inferred from trace element geochemistry of stromatolitic carbonates. Precambrian Res. 155, 229–250.

Bouma, A.H., 1962. Sedimentology of Some Flysch Deposits: A Graphic Approach to Facies Interpretation. Elsevier, 168 p.

Brasier, A.T., 2014. Archaean soils, lakes and springs: looking for signs of life. In: Dilek, Y., Furnes, H. (Eds.), Evolution of Archean Crust and Early Life. Springer Netherlands, Dordrecht, pp. 367–384.

Buick, R., 1992. The antiquity of oxygenic photosynthesis: evidence from stromatolites in sulphate-deficient Archaean lakes. Science 255, 74–77.

Cavalazzi, B., Barbieri, R., Gómez, F., Capaccioni, B., Olsson-Francis, K., Pondrelli, M., Rossi, A.P., Hickman-Lewis, K., Agangi, A., Gasparotto, G., Glamoclija, M., Ori, G.G., Rodriguez, N., Hagos, M., 2019. The Dallol geothermal area, northern Afar (Ethiopia)—an exceptional planetary field analog on Earth. Astrobiology 19, 553–578.

Crow, C., Condie, K.C., 1987. Geochemistry and origin of late Archean volcanic rocks from the Rhenosterhoek Formation, Dominion Group, South Africa. Precambrian Res. 37, 217–229.

Djokic, T., Van Kranendonk, M.J., Campbell, K.A., Walter, M.R., Ward, C.R., 2017. Earliest signs of life on land preserved in ca. 3.5 Ga hot spring deposits. Nat. Commun. 8, 15263.

Douglas, A.E., 2009. Endosymbionts and intracellular parasites. In: Schaechter, M. (Ed.), Encyclopedia of Microbiology, third edition. Academic Press, Oxford, pp. 128–141.

Eigenbrode, J.L., Summons, R.E., Steele, A., Freissinet, C., Millan, M., Navarro-González, R., Sutter, B., McAdam, A.C., Franz, H.B., Glavin, D.P., Archer, P.D., Mahaffy, P.R., Conrad, P.G., Hurowitz, J.A., Grotzinger, J.P., Gupta, S., Ming, D.W., Sumner, D.Y., Szopa, C., Malespin, C., Buch, A., Coll, P., 2018. Organic matter preserved in 3-billion-year-old mudstones at Gale crater, Mars. Science 360, 1096–1101.

Flannery, D.T., Allwood, A.C., Van Kranendonk, M.J., 2016. Lacustrine facies dependence of highly ^{13}C-depleted organic matter during the global age of methanotrophy. Precambrian Res. 285, 216–241.

Grandstaff, D.E., Edelman, M.J., Foster, R.W., Zbinden, E., Kimberley, M.M., 1986. Chemistry and mineralogy of Precambrian paleosols at the base of the Dominion and Pongola Groups (Transvaal, South Africa). Precambrian Res. 32, 97–131.

Guy, B.M., Ono, S., Gutzmer, J., Kaufman, A.J., Lin, Y., Fogel, M.L., Beukes, N.J., 2012. A multiple sulfur and organic carbon isotope record from non-conglomeratic sedimentary rocks of the Mesoarchean Witwatersrand Supergroup, South Africa. Precambrian Res. 216–219, 208–231.

Harris, A.C., White, N.C., McPhie, J., Bull, S., Line, M.A., Skrzeczynski, R., Mernagh, T., Tosdal, R.M., 2009. Early Archean hot springs above epithermal veins, North Pole, Western Australia: new insights from fluid inclusion microanalysis. Econ. Geol. 104, 793–814.

Hayes, J.M., 1994. Global methanotrophy at the Archean-Proterozoic transition. In: Bengston, S. (Ed.), Early Life on Earth. Nobel Symposium. Columbia University Press, New York, pp. 220–236.

Hedenquist, J.W., Lowenstern, J.B., 1994. The role of magmas in the formation of hydrothermal ore deposits. Nature 370, 519–527.

Homann, M., Sansjofre, P., Van Zuilen, M., Heubeck, C., Gong, J., Killingsworth, B., Foster, I.S., Airo, A., Van Kranendonk, M.J., Ader, M., Lalonde, S.V., 2018. Microbial life and biogeochemical cycling on land 3,220 million years ago. Nat. Geosci. 11, 665–671.

Iversen, N., Jorgensen, B.B., 1985. Anaerobic methane oxidation rates at the sulfate-methane transition in marine sediments from Kattegat and Skagerrak (Denmark). Limnol. Oceanogr. 30, 944–955.

Jackson, M.C., 1992. A review of the Late Archaean volcano-sedimentary Dominion Group and implications for the tectonic setting of the Witwatersrand Supergroup, South Africa. J. Afr. Earth Sci. 15, 169–186.

Jay, Z.J., Beam, J.P., Dlakić, M., Rusch, D.B., Kozubal, M.A., Inskeep, W.P., 2018. Marsarchaeota are an aerobic archaeal lineage abundant in geothermal iron oxide microbial mats. Nat. Microbiol. 3, 732–740.

Karhu, J.A., Bekker, A., 2020. Carbon isotopes in the solar system. In: Gargaud, M., et al. (Eds.), Encyclopedia of Astrobiology. Springer-Verlag, Germany.

Kida, K., Shigematsu, T., Kijima, J., Numaguchi, M., Mochinaga, Y., Abe, N., Morimura, S., 2001. Influence of Ni^{2+} and Co^{2+} on methanogenic activity and the amounts of coenzymes involved in methanogenesis. J. Biosci. Bioeng. 91, 590–595.

Konhauser, K.O., Lalonde, S.V., Planavsky, N.J., Pecoits, E., Lyons, T.W., Mojzsis, S.J., Rouxel, O.J., Barley, M.E., Rosiere, C., Fralick, P.W., Kump, L.R., Bekker, A., 2011. Aerobic bacterial pyrite oxidation and acid rock drainage during the Great Oxidation Event. Nature 478, 369–373.

Konhauser, K.O., Hao, W., Alessi, D.S., 2019. Acid weathering, clay transport and enhanced phosphate supply to early Paleoproterozoic oceans following the Great Oxidation Event. In: EGU General Assembly, EGU2019-6195.

Koschorreck, M., Wendt-Potthoff, K., Scharf, B., Richnow, H.H., 2008. Methanogenesis in the sediment of the acidic Lake Caviahue in Argentina. J. Volcanol. Geotherm. Res. 178, 197–204.

Krissansen-Totton, J., Arney, G.N., Catling, D.C., 2018. Constraining the climate and ocean pH of the early Earth with a geological carbon cycle model. Proc. Natl. Acad. Sci. 115, 4105.

Lepot, K., 2020. Signatures of early microbial life from the Archean (4 to 2.5 Ga) eon. Earth-Sci. Rev., 103296.

Löhr, A.J., Laverman, A.M., Braster, M., Van Straalen, N.M., Röling, W.F.M., 2006. Microbial communities in the world's largest acidic volcanic lake, Kawah Ijen in Indonesia, and in the Banyupahit river originating from it. Microb. Ecol. 52, 609–618.

Macfarlane, A.W., Danielson, A., Holland, H.D., 1994. Geology and major and trace element chemistry of late Archean weathering profiles in the Fortescue Group, Western Australia: implications for atmospheric PO_2. Precambrian Res. 65, 297–317.

Moernaut, J., De Batist, M., 2011. Frontal emplacement and mobility of sublacustrine landslides: results from morphometric and seismostratigraphic analysis. Mar. Geol. 285, 29–45.

Mossman, D.J., Minter, W.E.L., Dutkiewicz, A., Hallbauer, D.K., George, S.C., Hennigh, Q., Reimer, T.O., Horscroft, F.D., 2008. The indigenous origin of Witwatersrand "carbon". Precambrian Res. 164, 173–186.

Mukherjee, I., Large, R., 2017. Application of pyrite trace element chemistry to exploration for SEDEX style Zn-Pb deposits: McArthur Basin, Northern Territory, Australia. Ore Geol. Rev. 81 (Part 4), 1249–1270.

Mulkidjanian, A.Y., Bychkov, A.Y., Dibrova, D.V., Galperin, M.Y., Koonin, E.V., 2012. Origin of first cells at terrestrial, anoxic geothermal fields. Proc. Natl. Acad. Sci. 109, E821–E830.

Nabhan, S., Wiedenbeck, M., Milke, R., Heubeck, C., 2016. Biogenic overgrowth on detrital pyrite in ca. 3.2 Ga Archean paleosols. Geology 44, 763–766.

Neaman, A., Chorover, J., Brantley, S.L., 2005. Element mobility patterns record organic ligands in soils on early Earth. Geology 33, 117–120.

Nel, L.T., Jacobs, H., Allan, J.T., Bozzoli, G.R., 1937. Wonderstone. Geol. Surv. South Africa Bull. 8.

Petsch, S.T., 2014. Weathering of organic carbon. In: Treatise on Geochemistry, 2nd edition, pp. 217–238.

Pirajno, F., 2020. Subaerial hot springs and near-surface hydrothermal mineral systems past and present, and possible extraterrestrial analogues. Geosci. Front. 11, 1549–1569.

Rasmussen, B., Blake, T.S., Fletcher, I.R., Kilburn, M.R., 2009. Evidence for microbial life in synsedimentary cavities from 2.75 Ga terrestrial environments. Geology 37, 423–426.

Robb, L.J., Meyer, F.M., 1995. The Witwatersrand Basin, South Africa: geological framework and mineralization processes. Ore Geol. Rev. 10, 67–94.

Rye, R.O., Holland, H.D., 2000. Life associated with a 2.76 Ga ephemeral pond?: evidence from Mount Roe #2 paleosol. Geology 28, 483–486.

Sakurai, R., Ito, M., Ueno, Y., Kitajima, K., Maruyama, S., 2005. Facies architecture and sequence-stratigraphic features of the Tumbiana Formation in the Pilbara Craton, northwestern Australia: implications for depositional environments of oxygenic stromatolites during the Late Archean. Precambrian Res. 138, 255–273.

Schieber, J., 2007. Oxidation of detrital pyrite as a cause for marcasite formation in marine lag deposits from the Devonian of the eastern US. Deep-Sea Res., Part 2, Top. Stud. Oceanogr. 54, 1312–1326.

Schönheit, P., Moll, J., Thauer, R.K., 1979. Nickel, cobalt, and molybdenum requirement for growth of Methanobacterium thermoautotrophicum. Arch. Microbiol. 123, 105–107.

Schoonen, M.A.A., Barnes, H.L., 1991. Reactions forming pyrite and marcasite from solution: II. Via FeS precursors below 100 °C. Geochim. Cosmochim. Acta 55, 1505–1514.

Sforna, M.C., van Zuilen, M.A., Philippot, P., 2014. Structural characterization by Raman hyperspectral mapping of organic carbon in the 3.46 billion-year-old Apex chert, Western Australia. Geochim. Cosmochim. Acta 124, 18–33.

Shiki, T., Kumon, F., Inouchi, Y., Kontani, Y., Sakamoto, T., Tateishi, M., Matsubara, H., Fukuyama, K., 2000. Sedimentary features of the seismo-turbidites, Lake Biwa, Japan. Sediment. Geol. 135, 37–50.

Slotznick, S.P., Fischer, W.W., 2016. Examining Archean methanotrophy. Earth Planet. Sci. Lett. 441, 52–59.

Stüeken, E.E., Buick, R., 2018. Environmental control on microbial diversification and methane production in the Mesoarchean. Precambrian Res. 304, 64–72.

Teitler, Y., Philippot, P., Gérard, M., Le Hir, G., Fluteau, F., Ader, M., 2015. Ubiquitous occurrence of basaltic-derived paleosols in the Late Archean Fortescue Group, Western Australia. Precambrian Res. 267, 1–27.

Telford, R.J., Lamb, H.F., 1999. Groundwater-mediated response to Holocene climatic change recorded by the diatom stratigraphy of an Ethiopian crater lake. Quat. Res. 52, 63–75.

Thomazo, C., Ader, M., Farquhar, J., Philippot, P., 2009. Methanotrophs regulated atmospheric sulfur isotope anomalies during the Mesoarchean (Tumbiana Formation, Western Australia). Earth Planet. Sci. Lett. 279, 65–75.

Tiercelin, J.J., Gibert, E., Umer, M., Bonnefille, R., Disnar, J.R., Lézine, A.M., Hureau-Mazaudier, D., Travi, Y., Keravis, D., Lamb, H.F., 2008. High-resolution sedimentary record of the last deglaciation from a high-altitude lake in Ethiopia. Quat. Sci. Rev. 27, 449–467.

Wang, X., Ossa Ossa, F., Hofmann, A., Agangi, A., Paprika, D., Planavsky, N.J., 2020. Uranium isotope evidence for Mesoarchean biological oxygen production in shallow marine and continental settings. Earth Planet. Sci. Lett. 551, 116583.

Weissberg, B.G., 1969. Gold-silver ore-grade precipitates from New Zealand thermal waters. Econ. Geol. 64, 95.

Zeng, Z., Liu, X.-L., Wei, J.H., Summons, R.E., Welander, P.V., 2018. Calditol-linked membrane lipids are required for acid tolerance in Sulfolobus acidocaldarius. Proc. Natl. Acad. Sci. 115, 12932.

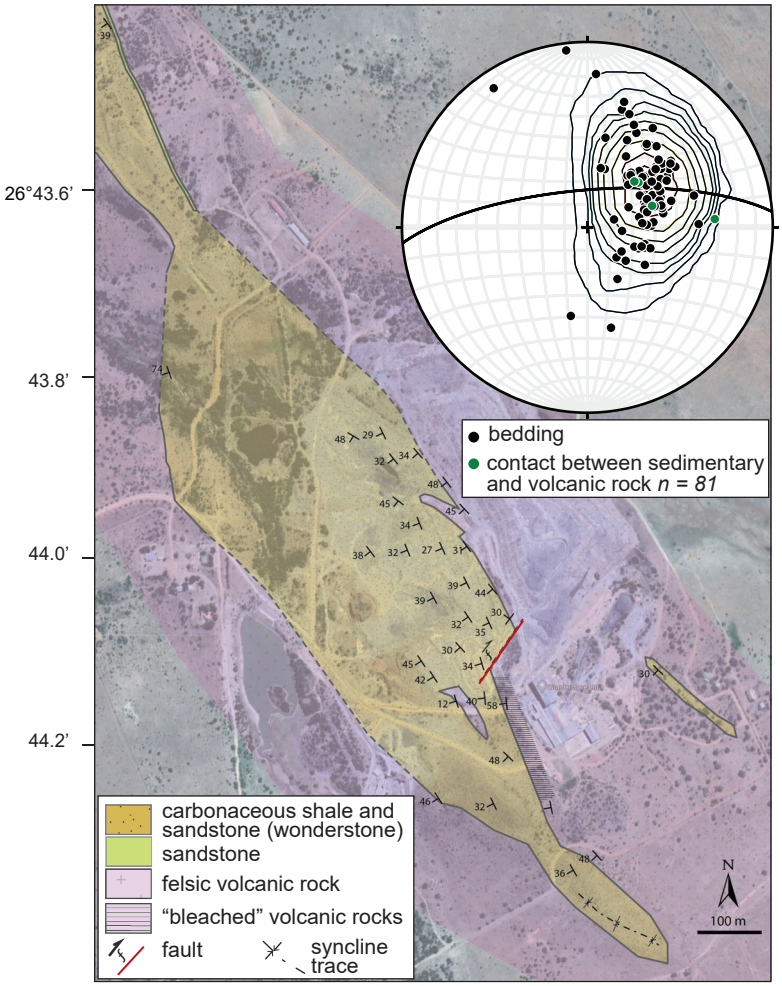

Supplementary Fig 1.

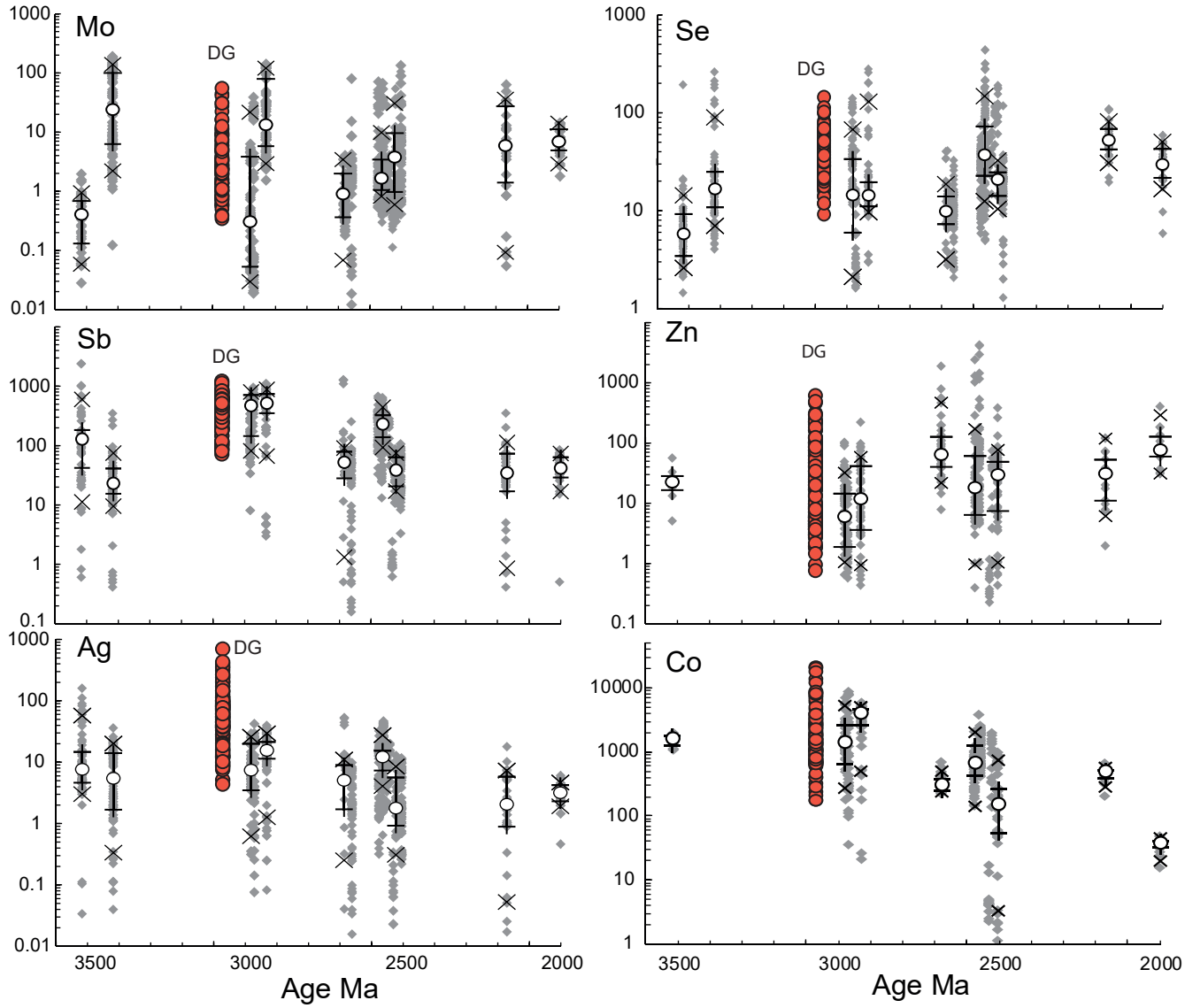

Supplementary Fig. 2

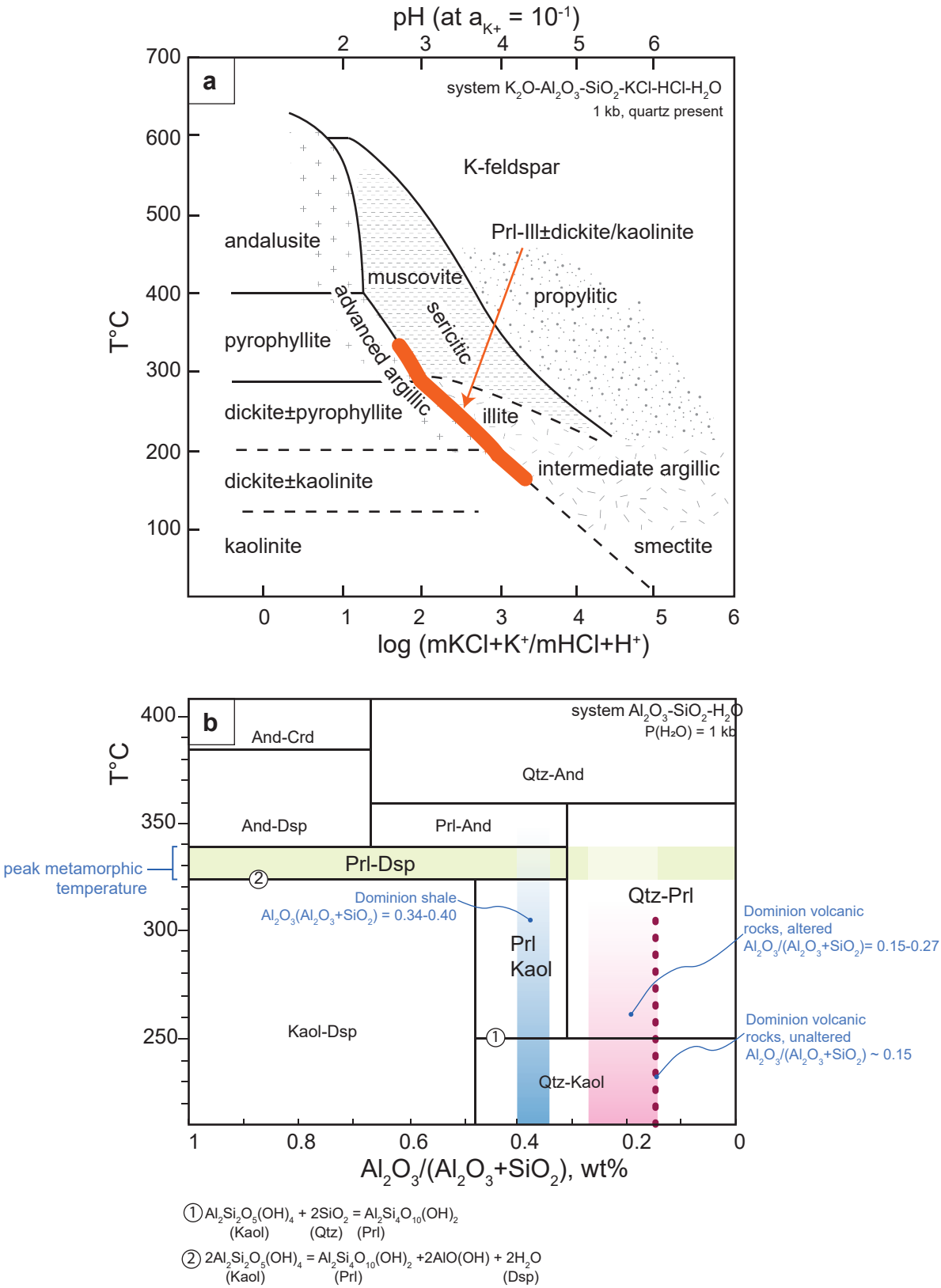

① $Al_2Si_2O_5(OH)_4$ + $2SiO_2$ = $Al_2Si_4O_{10}(OH)_2$
(Kaol) (Qtz) (Prl)

② $2Al_2Si_2O_5(OH)_4$ = $Al_2Si_4O_{10}(OH)_2$ + $2AlO(OH)$ + $2H_2O$
(Kaol) (Prl) (Dsp)

Supplementary Fig 3.

Supplementary Table 1. Whole-rock chemical analyses

	DWS-1	DWS-3	DWS-5	DWS-6A	DWS-7	DWS-10	DWS-11	DWS-13	DWS-14	DWS-8	DWS-9	DWS-32
rock	shale	shale	shale	shale	shale	tuff	tuff	feldspar porphyry	feldspar porphyry	feldspar porphyry	feldspar porphyry	altered volcanic
SiO2 (wr%)	59.80	56.22	53.02	55.51	55.62	74.15	73.25	70.09	71.79	72.81	73.54	67.81
Al2O3	30.22	32.80	35.81	33.87	32.35	13.36	11.71	12.60	12.30	12.09	12.22	24.74
Fe2O3T	0.39	0.86	0.13	0.23	1.66	5.16	4.09	7.56	5.56	4.30	3.69	bdl
MnO	bdl	bdl	bdl	bdl	0.01	0.02	0.11	0.06	0.06	0.06	0.04	bdl
MgO	0.03	0.05	0.05	0.06	0.17	1.32	0.75	0.91	0.63	0.58	0.43	0.00
CaO	0.02	0.02	0.02	bdl	0.01	0.06	2.38	0.28	0.36	0.56	0.45	0.06
Na2O	0.23	0.14	0.24	0.23	0.27	0.12	0.12	2.31	2.34	0.33	0.55	0.47
K2O	1.83	0.86	3.25	0.46	1.16	3.02	3.47	4.28	5.65	7.31	7.05	0.59
TiO2	1.57	1.87	1.63	1.95	1.95	0.51	0.46	0.68	0.45	0.49	0.44	1.07
P2O5	0.11	0.14	0.11	0.11	0.12	0.07	0.11	0.18	0.14	0.15	0.14	0.11
Cr2O3	0.02	0.02	0.03	0.02	0.03	0.01	bdl	0.01	bdl	0.06	0.02	bdl
L.O.I.	5.78	6.99	5.96	7.74	6.89	2.44	3.74	1.34	1.04	1.56	1.50	4.43
TOTAL	99.99	99.97	100.25	100.18	100.23	100.23	100.19	100.29	100.32	99.93	100.08	99.28
Sc (ppm)	6.17	8.03	1.75	2.20	5.52	1.74	4.59	6.64	4.72	4.20	4.31	12.39
V	197.08	264.03	141.91	209.92	300.23	6.91	11.06	12.05	11.92	11.73	9.54	20.48
Cr	92.88	126.12	83.98	77.47	124.17	7.27	5.65	7.12	8.77	3.28	17.19	3.14
Co	0.41	0.72	0.40	2.97	3.13	3.40	4.47	8.36	5.45	2.81	2.51	0.08
Ni	16.28	14.20	2.20	7.70	11.77	1.94	2.69	1.78	3.59	5.71	2.92	1.19
Cu	9.02	20.72	8.23	66.22	33.44	3.54	9.04	10.23	10.63	14.32	7.19	6.41
Zn	15.14	46.48	13.99	29.60	49.73	42.78	103.46	81.00	79.12	47.62	39.41	3.26
As	6.15	10.04	2.01	5.72	7.82	1.06	3.37	3.72	0.45	0.15	0.57	na
Rb	69.29	21.32	100.71	7.13	18.07	35.71	121.87	91.63	127.49	149.56	188.92	19.23
Sr	20.78	19.29	8.43	7.06	9.70	4.61	44.62	31.60	35.47	13.90	23.59	145.14
Y	10.84	4.60	2.77	0.54	0.79	8.59	27.36	22.22	18.00	29.72	24.22	106.33
Zr	500.08	542.76	680.98	571.95	493.57	251.31	235.82	260.47	349.47	357.93	334.92	1268.93
Nb	26.68	28.88	33.33	30.63	26.72	13.23	11.27	13.00	17.76	18.93	16.79	72.66
Ba	93.62	56.83	78.05	15.99	43.65	117.18	600.60	785.63	911.77	608.02	761.92	103.03
La	34.81	9.18	10.79	1.80	1.62	26.76	47.40	45.09	32.81	44.89	42.52	150.06
Ce	65.55	31.26	23.20	3.92	5.23	58.97	89.03	95.15	98.99	77.20	101.01	307.88
Pr	7.91	2.22	2.57	0.44	0.40	5.97	9.61	10.06	6.87	6.94	9.71	37.34
Nd	26.48	8.75	8.94	1.59	1.50	20.77	35.15	38.08	25.91	26.76	36.18	146.91
Sm	4.22	1.64	1.41	0.26	0.30	3.65	5.92	6.39	4.07	6.01	6.43	27.73
Eu	1.00	0.39	0.35	0.06	0.08	0.64	1.29	1.35	0.82	1.45	1.27	5.06
Gd	3.07	1.28	0.94	0.19	0.27	2.72	5.55	5.36	3.76	6.37	5.70	23.91
Tb	0.43	0.19	0.12	0.03	0.04	0.42	0.80	0.76	0.58	0.87	0.82	3.12
Dy	2.47	1.22	0.68	0.18	0.25	2.03	4.91	4.77	3.64	5.28	5.12	17.34
Ho	0.44	0.25	0.11	0.03	0.05	0.38	0.96	0.92	0.74	1.06	1.01	3.79
Er	1.12	0.73	0.30	0.09	0.16	1.06	2.62	2.55	2.15	3.03	2.86	11.01
Tm	0.16	0.11	0.04	0.01	0.02	0.16	0.36	0.38	0.33	0.50	0.42	1.82
Yb	0.99	0.74	0.25	0.09	0.17	1.01	2.16	2.34	2.12	3.16	2.71	12.72
Lu	0.13	0.11	0.03	0.01	0.03	0.14	0.32	0.34	0.32	0.47	0.39	1.91
Hf	12.41	13.31	16.45	13.78	12.21	6.22	5.73	6.45	8.66	9.01	8.15	30.60
Ta	1.63	1.85	2.29	1.91	1.71	0.80	0.69	0.73	1.15	1.23	1.09	4.32
W	5.92	6.47	6.55	3.21	12.71	0.26	0.32	0.36	0.32	0.45	0.37	0.53
Pb	11.21	17.14	15.58	15.05	14.94	6.13	179.19	9.26	8.60	9.20	9.91	9.76
Th	6.57	8.59	3.50	1.78	2.24	4.53	8.58	7.29	6.13	5.55	8.57	22.57
U	4.14	4.55	3.44	3.94	4.02	2.49	2.04	1.58	2.70	2.62	2.66	6.00
Mo	7.11	6.93	0.98	5.10	8.50	1.41	24.41	0.95	1.06	1.47	0.71	na

Supplementary Table 2. Chemical analyses of diagenetic pyrite (LA-ICP-MS). All concentrations as ppm

Analysis spot	texture	Mn	Co	Ni	Cu	Zn	As	Se	Mo	Ag	Sn	Sb	Au	Tl	Pb	Te
A-Rim-1	nodule rim	1.22	2016.6	745.3	262.9	3.61	111.5	22.55	0.80	38.93	0.96	614.8	1.05	2.91	292.7	2.33
A-Rim-2	nodule rim	1.36	997.0	889.6	251.7	3.82	65.3	22.45	0.74	55.62	1.05	801.7	0.93	2.53	408.0	3.56
A-Rim-3	nodule rim	1.21	997.7	987.4	224.6	2.67	120.1	26.26	0.81	53.12	0.97	787.9	0.83	3.43	422.5	2.42
A-Rim-4	nodule rim	2.71	1016.2	957.2	251.3	3.95	106.8	27.36	0.56	53.36	1.09	822.4	0.81	3.10	431.5	2.82
A-Rim-5	nodule rim	1.77	680.9	660.3	190.6	3.67	57.8	11.05	2.45	25.78	0.64	423.5	0.44	7.75	179.2	0.45
A-Rim-6	nodule rim	1.29	840.8	760.5	213.6	3.51	79.7	13.81	2.44	37.86	0.88	546.6	0.53	6.12	277.7	0.65
A-Rim-7	nodule rim	1.17	2709.4	809.3	230.7	2.86	288.4	22.62	1.95	46.60	0.83	670.5	0.72	3.50	349.2	1.10
A-Rim-8	nodule rim	1.33	2607.5	800.6	226.5	2.99	213.5	20.99	0.97	43.02	0.87	637.2	0.77	2.34	346.7	0.93
A-Rim-9	nodule rim	1.23	1110.9	787.4	281.9	4.44	124.6	16.93	1.36	33.55	0.75	580.9	0.55	4.93	260.6	0.38
A-Rim-10	nodule rim	1.15	1093.4	893.5	594.6	5.80	85.3	20.00	1.50	44.62	1.46	686.0	0.74	4.67	331.7	1.45
A-Rim-11	nodule rim	2.08	1006.5	954.1	263.2	3.86	117.3	23.27	0.65	53.71	1.53	775.2	0.91	3.77	437.3	1.16
A-Rim-12	nodule rim	1.15	912.8	890.9	359.6	3.23	64.9	20.01	1.15	36.30	0.91	590.8	0.58	6.45	292.0	2.79
A-Rim-13	nodule rim	1.33	831.7	870.4	232.9	3.18	49.7	17.94	1.34	35.99	0.81	576.4	0.59	7.30	247.1	1.94
A-Rim-14	nodule rim	1.39	1025.7	834.6	250.4	2.59	37.6	15.87	1.16	45.49	0.95	681.9	0.75	4.79	314.1	0.25
A-Rim-15	nodule rim	1.42	948.9	749.6	238.0	2.98	40.9	12.35	1.34	38.91	1.00	600.1	0.56	4.45	260.2	0.18
A-Core-1	nodule core	2.07	580.1	555.2	141.4	4.17	49.5	17.18	1.04	68.70	0.76	533.3	1.31	1.17	444.9	0.25
A-Core-2	nodule core	3.05	634.3	647.4	161.7	5.47	63.1	17.78	0.73	80.46	0.93	608.0	1.39	1.53	519.0	0.31
A-Core-3	nodule core	2.66	695.1	705.3	167.9	4.97	62.8	18.98	0.87	92.72	1.10	659.4	1.53	1.84	559.0	0.39
A-Core-4	nodule core	4.16	660.8	634.3	156.2	5.76	55.6	19.67	0.73	72.75	0.94	574.8	1.08	1.50	456.5	0.33
A-Core-5	nodule core	5.12	692.3	694.0	165.6	7.17	65.9	20.08	0.69	78.06	0.94	632.4	1.42	1.68	498.7	0.36
A-Core-6	nodule core	2.43	754.2	671.5	162.6	5.66	92.3	20.46	1.01	81.33	0.94	607.7	1.46	1.62	511.8	<0.19
A-Core-7	nodule core	2.79	667.3	683.6	158.6	6.17	70.2	18.74	1.01	80.05	0.93	617.8	1.64	1.36	496.8	<0.09
A-Core-8	nodule core	2.51	648.4	688.2	163.9	4.40	64.7	20.00	1.07	83.57	1.00	621.7	1.46	1.39	504.4	<0.13
A-Core-9	nodule core	2.77	654.1	670.9	162.9	5.93	61.0	19.75	0.84	85.64	0.94	619.5	1.55	1.24	498.9	<0.14
A-Core-10	nodule core	2.68	689.3	725.9	189.0	6.91	55.1	22.70	0.97	98.53	1.08	669.8	1.87	0.95	608.1	0.16
A-Core-11	nodule core	5.70	682.1	736.0	188.7	7.87	58.3	21.13	0.78	91.68	1.11	655.4	1.54	1.86	568.0	<0.05
A-Core-12	nodule core	4.21	652.5	670.9	175.0	5.75	50.8	16.51	0.81	89.79	1.06	634.2	1.51	1.39	531.2	0.12
A-Core-13	nodule core	3.21	749.4	816.8	192.1	4.63	72.7	23.52	0.58	102.44	1.28	737.9	1.93	1.14	738.6	0.15
A-Core-14	nodule core	3.37	650.8	663.5	151.3	6.13	64.7	18.61	0.89	75.23	0.98	615.4	1.46	1.20	541.8	0.19
A-Core-15	nodule core	3.54	705.3	776.3	171.4	10.54	80.6	22.37	0.60	92.90	1.19	693.2	1.67	1.21	626.8	0.10
A-CoreIR-1	nodule core	1.31	813.2	626.4	222.0	4.43	62.0	17.62	0.34	40.54	0.84	582.0	0.76	0.44	275.6	0.23
A-CoreIR-2	nodule core	1.17	7174.5	698.1	452.9	6.93	612.1	30.85	1.18	49.02	1.24	650.9	1.02	0.61	369.8	0.13
A-CoreIR-3	nodule core	0.86	13294.8	321.5	80.6	1.89	1492.0	29.06	0.59	28.06	0.52	323.5	0.59	0.15	231.3	0.09
A-CoreIR-4	nodule core	1.19	1280.0	957.7	204.3	4.04	125.0	31.90	0.56	72.41	1.31	845.4	1.43	0.27	510.9	0.24
A-CoreIR-5	nodule core	1.50	1279.2	1067.4	205.2	4.35	143.4	33.16	0.50	80.55	1.39	899.4	1.72	0.35	545.7	0.36
A-CoreIR-6	nodule core	1.25	1051.3	905.8	188.3	4.12	107.5	24.26	0.70	66.54	1.02	823.0	1.22	0.33	454.4	<0.15
A-CoreIR-7	nodule core	2.04	1081.4	1006.7	247.8	8.12	448.9	33.16	3.24	73.32	1.78	781.7	1.49	2.22	545.9	0.31
A-CoreIR-8	nodule core	1.33	2247.8	1087.3	263.1	4.90	202.6	36.52	3.23	86.51	1.60	1046.5	1.66	0.43	591.0	0.33
A-CoreIR-9	nodule core	2.97	853.5	898.6	172.4	5.56	191.4	23.53	1.37	73.77	1.10	640.4	1.44	1.67	557.3	0.15
A-CoreIR-10	nodule core	0.98	1664.4	1399.0	273.1	4.84	141.9	40.09	2.39	113.40	1.77	1248.7	2.05	0.52	740.0	0.31
A-CoreIR-11	nodule core	1.73	1322.7	1152.1	251.2	5.24	142.0	29.50	2.70	70.83	1.54	897.0	1.21	1.83	502.8	0.16

A-CoreIR-12	nodule core	1.60	3158.8	1246.7	264.4	4.39	422.6	49.48	1.36	111.17	2.62	1156.8	2.25	0.18	825.4	0.52
A-CoreIR-13	nodule core	1.05	1860.3	417.0	180.7	4.80	177.9	12.02	0.39	23.85	0.60	368.6	0.43	0.01	172.4	<0.10
A-CoreIR-14	nodule core	1.12	1502.4	958.6	301.5	3.64	121.9	23.79	0.38	62.29	0.99	764.5	1.11	0.03	422.8	0.26
A-CoreIR-15	nodule core	0.72	20527.6	304.6	100.5	1.85	1999.8	54.20	7.49	39.98	2.98	331.2	0.66	0.13	318.3	<0.08
DWS6KA-1	fine-grained	44.76	1330.5	149.4	263.8	9.46	229.4	31.05	6.73	12.10	1.56	302.1	0.13	7.77	1193.9	0.48
DWS6KA-2	fine-grained	7.52	7941.9	381.1	84.3	7.87	585.5	79.80	2.27	44.56	2.06	91.5	0.07		210.8	<2.64
DWS6KA-3	fine-grained	0.81	1306.6	1635.0	325.6	3.58	3670.8	39.64	2.41	5.09	0.32	147.8	0.04	2.64	765.3	0.34
DWS6KA-4	fine-grained	0.72	2984.4	1115.2	342.3	0.93	10191.2	32.64	6.80	7.48	0.24	104.0	0.09	1.72	504.4	0.78
DWS6KA-5	fine-grained	1.95	3311.3	1670.3	370.7	2.88	8177.6	31.09	8.43	8.43	0.33	121.1	0.09	2.05	728.3	0.72
DWS6KA-6	fine-grained	1.38	1695.0	4741.8	2436.1	9.44	970.0	41.39	4.75	22.75	27.08	379.6	0.31	10.43	2455.1	0.59
DWS6KA-7	fine-grained	0.70	3690.7	2523.3	363.5	0.74	4227.8	52.74	10.87	4.34	0.41	116.4	0.04	1.99	571.5	0.57
DWS6KA-8	fine-grained	6.12	1238.8	266.0	142.5	8.50	217.7	34.41	1.05	25.55	1.30	254.8	0.05	7.32	958.6	0.39
DWS6KA-9	fine-grained	3.01	756.4	189.0	139.6	8.71	187.1	34.59	0.83	8.87	7.40	265.9	0.06	8.39	1088.5	0.24
DWS6KA-10	fine-grained	4.24	1469.8	208.2	183.5	4.83	262.6	30.58	1.18	9.82	0.99	197.9	0.04	5.33	729.2	0.26
DWS6KA-11	fine-grained	15.12	2481.4	193.5	124.4	59.96	264.7	38.13	2.44	37.08	1.38	176.2	0.06	4.32	727.1	0.18
DWS6KA-12	fine-grained	9.54	8025.5	353.6	108.7	13.54	563.3	57.67	2.00	13.45	1.34	104.4	0.07	1.88	386.9	0.12
DWS6KA-13	fine-grained	2.08	1742.9	278.6	167.6	16.24	420.0	31.42	2.68	8.85	1.47	251.8	0.13	6.04	1029.8	0.33
DWS6KA-14	fine-grained	2.80	799.8	283.7	189.3	8.38	261.1	31.23	2.63	12.22	1.34	281.1	0.09	7.82	1124.9	0.25
DWS6KA-15	fine-grained	59.03	3840.8	142.6	220.3	453.44	357.0	35.61	5.99	173.18	3.77	194.2	0.13	6.03	753.4	1.01
DWS6KA-16	fine-grained	4.26	6783.6	270.3	140.1	16.35	436.0	41.54	1.55	13.06	1.67	148.1	0.08	2.25	455.8	0.40
DWS6KA-17	fine-grained	10.76	1998.6	254.4	355.2	99.37	302.7	24.72	3.75	27.97	2.21	341.6	0.13	4.79	1117.6	0.53
DWS6KA-18	fine-grained	19.69	3356.6	398.6	270.1	21.51	382.7	30.69	2.18	36.03	1.88	187.3	0.15	3.41	614.1	0.85
DWS6KA-19	fine-grained	4.11	1825.7	71.4	183.1	19.33	255.1	25.84	1.81	15.72	1.19	232.9	0.05	6.88	792.3	<0.11
DWS6KA-20	fine-grained	3.67	2300.5	183.3	167.2	38.38	224.7	26.55	9.42	17.30	1.55	202.4	0.14	5.04	747.0	0.39
DWS6KA-21	fine-grained	8.06	657.7	57.9	270.5	12.58	56.4	12.37	1.97	16.23	1.18	181.6	0.03	5.37	563.1	0.12
DWS6KA-22	fine-grained	10.32	5680.5	331.7	160.9	286.72	728.0	37.79	8.62	9.64	0.95	114.5	0.07	2.99	496.4	<0.12
DWS6KA-23	fine-grained	8.70	1847.6	87.1	365.0	26.91	277.0	26.66	2.87	27.75	1.23	216.5	0.08	4.78	682.9	0.48
DWS6KA-24	fine-grained	8.45	2514.8	108.4	297.3	24.29	343.0	29.25	16.26	98.12	1.64	196.0	0.10	4.94	761.5	0.50
DWS6KA-25	fine-grained	73.79	2434.5	183.7	228.1	46.04	414.9	27.91	1.60	345.37	1.67	183.1	0.09	4.26	590.5	0.62
DWS6KA-26	fine-grained	17.81	1423.1	96.1	243.2	96.30	134.2	18.18	9.15	100.17	1.77	205.9	0.08	6.60	724.5	0.40
DWS6KA-27	fine-grained	9.33	2755.5	191.6	398.6	22.05	303.4	31.14	2.26	36.48	1.42	233.8	0.13	6.09	1062.9	0.69
DWS6KA-28	fine-grained	2.65	2311.9	145.3	197.9	9.49	365.6	28.31	5.06	15.63	1.61	251.1	0.10	6.19	766.3	0.50
DWS6KA-30	fine-grained	25.34	1556.3	87.2	366.8	72.56	325.5	22.72	9.24	85.28	3.65	208.4	0.09	5.73	811.2	0.53
DWS6KB-1	fine-grained	1.42	8113.1	821.9	271.2	1.75	13818.9	49.62	27.50	11.51	0.35	88.0	0.13	1.31	407.7	0.65
DWS6KB-2	fine-grained	4.01	6248.8	1865.6	197.0	2.84	12895.2	53.02	44.08	12.74	1.03	85.7	0.10	2.12	522.3	0.39
DWS6KB-5	fine-grained	14.13	2609.8	1003.0	264.1	16.56	3680.7	35.03	22.27	62.16	0.46	249.7	0.09	5.56	1392.6	0.38
DWS6KB-6	fine-grained	9.36	986.1	868.7	842.9	17.71	308.7	31.21	41.01	32.69	2.19	563.1	0.61	37.70	220.5	5.31
DWS6KB-10	fine-grained	53.43	1787.0	659.6	457.7	90.65	5509.3	<77.87	55.13	705.30	14.94	265.2	0.49	10.95	2243.5	3.76
DWS6KB-11	fine-grained	92.67	11627.0	3988.1	1735.9	241.09	570.0	129.68	30.90	309.24	21.91	235.8	0.67	7.48	1955.2	<1.81
DWS6KB-14	fine-grained	11.30	7366.2	4920.4	1984.9	32.97	808.1	<60.52	15.85	62.47	11.44	233.4	0.62	7.79	2240.6	<1.82
DWS6N-1	fine-grained	8.11	949.9	200.9	212.5	67.04	259.0	26.96	9.98	39.48	3.82	440.4	0.32	21.73	853.8	0.40
DWS6N-2	fine-grained	10.25	743.1	728.4	513.3	60.72	5056.0	24.71	7.29	32.78	1.30	186.9	0.22	4.28	1217.0	0.46
DWS6N-3	fine-grained	136.62	1476.2	541.1	746.2	598.87	784.6	44.68	5.00	242.09	3.30	464.6	0.38	25.50	1409.3	0.70
DWS6N-5	fine-grained	7.76	3620.5	675.7	151.5	45.56	521.7	35.71	1.02	44.96	1.59	269.7	0.26	6.10	864.7	0.95
DWS6N-6	fine-grained	6.50	4392.8	664.2	167.5	19.66	1284.5	39.31	1.37	50.11	1.76	316.8	0.30	11.97	1206.4	0.61

DWS6N-7	fine-grained	80.83	597.0	384.1	437.3	223.73	375.1	32.72	4.66	265.64	3.21	536.4	0.31	27.76	1624.0	0.59
DWS6N-8	fine-grained	30.38	627.3	115.7	274.9	98.89	302.2	22.75	8.81	112.89	4.38	405.7	0.22	22.10	931.2	0.67
DWS6N-9	fine-grained	27.91	1365.3	400.5	351.0	85.64	317.2	31.87	2.87	133.78	1.95	378.2	0.23	22.63	723.3	1.08
DWS6N-10	fine-grained	38.59	1057.9	189.2	464.7	199.88	688.5	30.41	11.19	142.84	7.39	856.0	0.60	38.46	2023.0	1.54
DWS6N-11	fine-grained	18.76	630.6	138.4	390.8	45.71	1657.7	27.42	3.11	59.79	1.78	521.8	0.20	26.40	1678.2	0.69
DWS6N-12	fine-grained	2.71	165.6	141.1	299.2	5.02	930.9	67.28	1.54	20.43	0.88	430.0	0.12	29.46	1578.8	0.37
DWS6N-13	fine-grained	2.89	309.4	138.6	109.5	5.08	147.6	13.30	1.15	12.11	0.91	313.0	0.11	21.37	581.3	0.28
DWS6N-15	fine-grained	95.44	387.2	189.0	477.1	303.10	214.3	25.79	3.48	399.02	4.35	567.5	0.29	34.94	1172.1	0.37
DWS6N-16	fine-grained	11.78	223.7	137.4	305.5	12.80	958.9	15.99	1.60	202.60	1.02	471.0	0.11	35.83	1263.6	0.28
DWS6N-17	fine-grained	9.68	4842.5	1136.4	301.4	6.78	2396.6	58.21	1.40	19.66	1.43	111.7	0.08	4.51	567.5	0.13
DWS6N-18	fine-grained	27.68	385.3	244.6	454.2	39.11	2620.3	41.28	2.66	55.80	0.70	182.2	0.13	3.96	957.9	0.35
DWS6N-19	fine-grained	47.85	900.7	539.0	587.7	217.50	306.9	29.94	3.59	239.32	2.30	438.4	0.18	20.40	1458.9	0.52
DWS6N-20	fine-grained	35.13	8466.3	402.1	246.8	117.44	2296.2	53.81	2.77	197.05	2.10	315.0	0.19	12.12	867.3	0.57
DWS6N-21	fine-grained	28.50	1055.1	596.9	386.8	101.56	513.2	33.04	2.09	145.94	2.78	415.6	0.20	16.16	1462.4	0.40
DWS6N-22	fine-grained	1.43	7997.3	916.2	426.6	4.05	3219.7	76.36	1.37	8.13	0.43	100.1	0.08	1.08	568.5	0.19
DWS6N-23	fine-grained	85.21	2513.6	1240.5	556.6	218.68	645.2	43.96	16.48	364.06	10.32	727.2	0.27	19.51	1931.5	<1.16
DWS6N-24	fine-grained	9.47	3773.0	1178.8	248.6	30.11	1226.0	49.36	1.91	86.08	1.70	247.3	39.39	7.42	1459.4	0.49
DWS6N-25	fine-grained	38.65	862.0	334.2	288.1	157.70	428.3	29.41	2.36	121.86	1.78	461.8	0.22	26.07	1627.4	0.27
DWS6N-26	fine-grained	90.62	1559.9	660.0	294.5	59.56	759.7	28.98	2.45	98.55	1.88	407.9	0.30	20.15	1479.7	0.38
DWS6N-27	fine-grained	24.75	1568.9	456.8	338.2	81.82	648.1	41.08	3.56	69.16	2.06	450.7	0.16	21.38	1720.3	0.47
DWS6N-28	fine-grained	38.66	938.4	1241.6	224.5	50.71	735.5	54.57	11.53	81.19	5.57	478.5	0.24	16.33	1520.1	<1.08
DWS6N-29	fine-grained	33.98	585.7	241.4	222.9	117.48	290.0	26.97	3.46	102.08	2.71	445.6	0.79	26.42	1070.1	0.83
DWS6N-30	fine-grained	21.39	2877.5	316.3	329.3	41.54	451.3	44.02	3.39	76.00	2.51	387.9	0.13	12.17	1502.9	0.52
DWS6N-31	fine-grained	1.65	19461.7	352.6	104.8	2.11	4502.0	120.66	5.92	11.89	2.14	72.5	0.12	0.43	163.1	1.04
DWS6N-32	fine-grained	59.13	3185.9	590.0	475.9	97.84	3212.8	101.61	5.08	212.13	11.42	120.1	<0.40	5.52	1457.1	7.46
DWS6N-33	fine-grained	38.45	1205.8	830.8	306.0	24.92	1342.8	40.18	2.33	36.97	1.69	315.4	0.08	13.95	1692.0	0.13
DWS6N-34	fine-grained	0.72	17099.8	418.9	136.8	1.42	5068.5	103.80	12.49	14.82	0.21	81.1	0.13	0.56	241.5	0.95
DWS6N-35	fine-grained	9.23	1706.4	883.6	385.5	83.38	1134.3	33.03	30.72	56.04	5.07	349.7	0.12	13.19	2217.5	0.76
DWS6N-36	fine-grained	2.37	1435.9	479.2	530.2	33.01	2753.7	43.07	3.76	14.16	1.95	477.4	0.08	21.00	2011.1	0.82
DWS6N-37	fine-grained	2.63	434.9	1008.6	197.5	3.54	723.2	29.95	3.17	10.12	1.99	306.5	0.12	16.77	1825.8	0.26
DWS6N-38	fine-grained	7.05	923.6	617.7	394.7	7.74	1324.0	46.03	4.85	38.84	2.83	311.2	0.06	12.92	1815.1	<0.51
DWS6N-39	fine-grained	47.18	1222.0	324.0	287.9	158.48	272.7	26.72	2.27	169.59	1.91	336.2	0.21	24.60	588.6	0.45
DWS6N-40	fine-grained	11.87	633.4	301.5	439.5	124.02	2804.7	33.80	2.26	41.14	1.65	361.1	0.13	22.12	1508.1	0.36
DWS6N-41	fine-grained	35.66	1371.8	381.1	471.4	177.41	551.9	27.82	4.10	431.77	1.91	395.1	0.26	23.17	814.0	0.51
DWS6N-42	fine-grained	28.42	696.6	193.0	449.4	120.37	548.3	19.19	3.31	146.79	2.67	510.5	0.34	28.16	959.8	0.64
DWS6N-43	fine-grained	17.15	781.3	186.5	372.4	73.60	584.2	21.19	3.36	54.32	4.25	490.0	0.19	37.10	1350.0	0.50
DWS6N-44	fine-grained	14.35	3694.8	178.6	191.5	476.91	758.1	27.68	2.00	49.40	1.65	298.7	0.09	18.38	747.3	0.40
DWS6N-45	fine-grained	14.03	1344.9	543.6	200.4	52.64	351.2	26.31	1.08	38.07	0.86	343.4	0.11	26.29	888.4	0.40
DWS6N-46	fine-grained	13.58	200.7	116.7	222.1	19.46	523.8	20.56	2.24	18.38	0.91	432.6	0.09	35.84	1153.2	0.30
DWS6N-47	fine-grained	70.95	1282.6	134.0	344.5	288.96	279.1	31.67	5.76	268.20	5.04	482.3	0.90	26.39	1015.9	0.76
DWS6N-48	fine-grained	39.95	1483.3	240.8	252.7	40.40	342.7	36.40	5.31	77.25	3.88	564.7	0.47	27.82	1061.2	<0.17
DWS6N-49	fine-grained	52.60	275.0	130.5	255.4	73.88	577.0	26.19	7.46	59.46	2.94	626.6	0.27	38.47	2064.4	0.83
DWS6N-50	fine-grained	8.35	167.3	126.3	423.4	33.20	756.3	54.91	4.63	44.38	2.07	607.3	0.23	37.27	1567.1	0.43
DWS6N-51	fine-grained	9.66	2164.6	279.0	218.6	83.24	458.5	32.92	5.10	61.23	3.45	521.6	0.50	21.44	1523.2	0.42